FACULTÉ DES ÉTUDES SUPÉRIEURES
ET POSTOCTORALES

uOttawa

L'Université canadienne
Canada's university

FACULTY OF GRADUATE AND
POSDOCTORAL STUDIES

Clare McElcheran
AUTEUR DE LA THÈSE / AUTHOR OF THESIS

M.Sc. (Physics)
GRADE / DEGREE

Department of Physics
FACULTÉ, ÉCOLE, DÉPARTEMENT / FACULTY, SCHOOL, DEPARTMENT

Understanding Femtosecond Laser Modifications of Bulk Dielectrics
TITRE DE LA THÈSE / TITLE OF THESIS

L. Ramunno
DIRECTEUR (DIRECTRICE) DE LA THÈSE / THESIS SUPERVISOR

CO-DIRECTEUR (CO-DIRECTRICE) DE LA THÈSE / THESIS CO-SUPERVISOR

P. Corkum

R. Williams

J. Armitage

Gary W. Slater
Le Doyen de la Faculté des études supérieures et postdoctorales / Dean of the Faculty of Graduate and Postdoctoral Studies

Understanding Femtosecond Laser Modification of Bulk Dielectrics

Clare McElcheran

Thesis submitted to the
Faculty of Graduate and Postdoctoral Studies
In partial fulfillment of the requirements
For the MSc degree in Physics

Department of Physics
Faculty of Graduate and Postdoctoral Studies
University of Ottawa

Library and Archives
Canada

Published Heritage
Branch

395 Wellington Street
Ottawa ON K1A 0N4
Canada

Bibliothèque et
Archives Canada

Direction du
Patrimoine de l'édition

395, rue Wellington
Ottawa ON K1A 0N4
Canada

Your file Votre référence
ISBN: 978-0-494-69071-0
Our file Notre référence
ISBN: 978-0-494-69071-0

NOTICE:

The author has granted a non-exclusive license allowing Library and Archives Canada to reproduce, publish, archive, preserve, conserve, communicate to the public by telecommunication or on the Internet, loan, distribute and sell theses worldwide, for commercial or non-commercial purposes, in microform, paper, electronic and/or any other formats.

The author retains copyright ownership and moral rights in this thesis. Neither the thesis nor substantial extracts from it may be printed or otherwise reproduced without the author's permission.

AVIS:

L'auteur a accordé une licence non exclusive permettant à la Bibliothèque et Archives Canada de reproduire, publier, archiver, sauvegarder, conserver, transmettre au public par télécommunication ou par l'Internet, prêter, distribuer et vendre des thèses partout dans le monde, à des fins commerciales ou autres, sur support microforme, papier, électronique et/ou autres formats.

L'auteur conserve la propriété du droit d'auteur et des droits moraux qui protège cette thèse. Ni la thèse ni des extraits substantiels de celle-ci ne doivent être imprimés ou autrement reproduits sans son autorisation.

In compliance with the Canadian Privacy Act some supporting forms may have been removed from this thesis.

While these forms may be included in the document page count, their removal does not represent any loss of content from the thesis.

Conformément à la loi canadienne sur la protection de la vie privée, quelques formulaires secondaires ont été enlevés de cette thèse.

Bien que ces formulaires aient inclus dans la pagination, il n'y aura aucun contenu manquant.

Canada

Contents

List of Figures

Abstract

The minimum spacing of a plasma waveguide was calculated and applied to the formation of periodic nanocracks. The minimum spacing decreased with decreasing plasma frequency but was found to have limited effect on the spacing of the nanocracks.

An extension to a standard Finite-Difference Time-Domain method was created to include nonlinear processes and the dynamic build up of the electron plasma. The ionized area produced in the simulation agrees with experiment. The existence of a self-limited absorption effect on a Gaussian pulse in time was verified in the simulations. The region was elongated along the direction parallel to the polarization of the light. The multiphoton absorption was found to be the main cause of the distinct shape of the damaged area. Plasma dispersion and self-focusing create larger electron densities and a shift in the location of the electron density peak, but did not affect the general shape.

Acknowledgements

I would like to thank my supervisor, Dr. Lora Ramunno, for her support and guidance. Without her dedication and encouragement this thesis could not have been completed. I would also like to thank Dr. Paul Corkum for his collaboration. His insight into the experimental applications of our simulations helped to shape the results of this thesis.

I would like to thank Nicolas Bigaouette and Dr. Edward Ackad for their contributions through discussions and technical support. I would also like to thank Mr. Bigaouette for his assistance with diagrams. Finally, I would like to thank Grant Middleton for his constant support.

Chapter 1

Introduction

In the past decade, ultrafast lasers have enabled new techniques for the micromachining of materials. The advent of femtosecond pulses has allowed light to reach extremely high intensities, high enough to excite nonlinear processes, such as multiphoton ionization. Since dielectric materials are transparent to light in the low intensity (linear) regime, femtosecond pulses can be focused within the bulk of a dielectric. Dielectric modification via nonlinear absorption only occurs where the intensity is highest, near the focus. Various forms of dielectric modification, or "damage" can be created, including an index of refraction change [24], void-like structures [21] or periodically spaced cracks inside the modified region [4], depending on the laser fluence, repetition rate and pulse duration, and the material itself. This highly controlled damage within the bulk can be used for many applications where the machining capability in three dimensions is highly desirable, such as the fabrication of 3D photonic crystals, microfluidic devices, volume gratings, optical memories and optical waveguides [69, 20].

Though there is a basic understanding of the processes which cause the damage, it is difficult to predict a priori which nonlinear processes would be important in each situation. This thesis will address this issue through numerical simulations. In recent years, there has been some theoretical work that attempts to determine the importance of different nonlinear processes in each regime [47, 51, 45, 28]. This thesis will build on this theory by incorporating nonlinear processes and macroscopic properties of dielectrics into three-dimensional simulations. In this chapter, we review some of the experiments done in this field, the processes underlying nonlinear ionization and material modification, and the current theories of the formation of nanocracks. We then introduce the focus of this thesis including the contributions to the field and the organization of this thesis.

1.1 Experimental Results

In order to create the regions of modified index of refraction, an intense, femtosecond laser is focused inside a dielectric. The laser has a fixed repetition rate, but the dielectric sample can either be moved at a constant rate or remain fixed. When the sample is translated relative to the writing laser, a waveguide is created [41, 17]. When the position is fixed, a microlens or a voxel for data storage is created [21, 68].

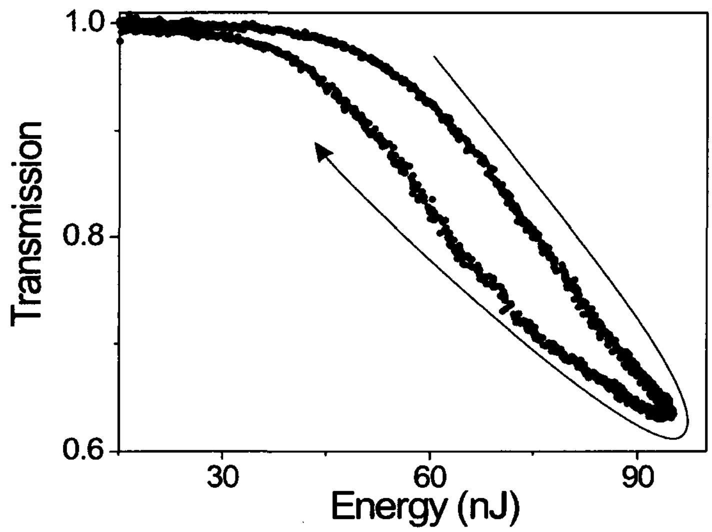

Figure 1.1: *Memory Effect in Dielectrics (from [49])*

The modified structure is usually created over a series of pulses or shots. This is possible because the dielectric exhibits a memory of the ionization of the previous pulse. While electrons within the dielectric are ionized during the laser pulse, they are eventually trapped in the region of the parent ion after the pulse [3]. The region that was ionized experiences chemical changes which lower the ionization potential. This process provides a feedback loop for ionization that allows structures to build over many shots. This memory of the material has been observed to create a reduction of the threshold intensity [49] (Fig. 1.1)

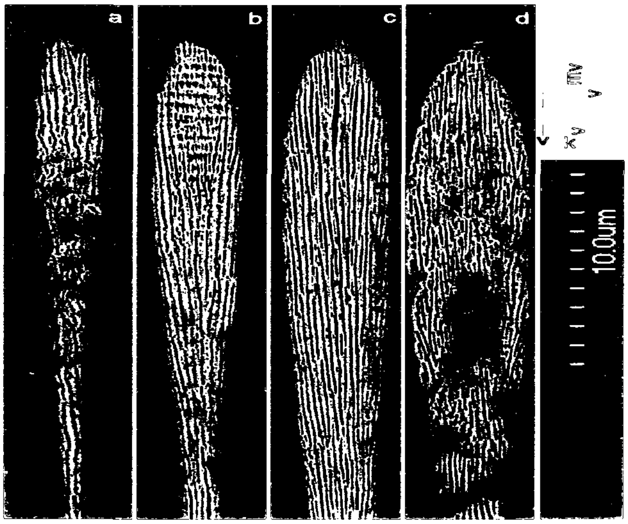

Figure 1.2: *Modified region observed in experiment for increasing numbers of shots. Least number of shots in (a) to most number of shots in (d). The region grows wider and longer over many shots.(from [23])*

For laser pulses focused within a dielectric, the modified region evolves into a long shape with a rounded tip and tapered end [68]. With increasing numbers of laser shots, the shape is seen to become longer and wider (Fig. 1.2). The resulting shape is either confined to a carrot-like shape by irradiating the same region over many shots or elongated into a trench by translating the sample or laser at a constant rate.

There are three laser parameters that are found to influence the morphology of the damaged region: the repetition rate, the pulse length and the energy. The regime of interest for this thesis is that of low repetition rates (1-200 KHz), short pulses (1-200 fs) and low (150 nJ) to medium (300 nJ) pulse energies. Low repetition rates allow the sample to cool between pulses limiting the effect of thermal accumulation. The effect of a short pulse duration is to create higher intensities at the focus, so that multiphoton ionization becomes the dominant process that brings electrons into the conduction bad. For laser pulses focused on the surface, short pulses are known to create damage areas (craters) that are much more regular in appearance, and do not affect adjacent areas [35]. A short pulse duration is also thought to limit the contribution of avalanche ionization (though it is unknown to what extent). In the low energy regime, the modified region has a uniform change (increase) in the refractive index. As the energy deposited into the region increases, periodic nanocracks are observed. Due to the directionality of the cracks, there is also some degree of form birefringence.

Because of the shape of the modified region, it can behave as a biconvex micro-lens. By focusing a Gaussian beam into the modified region and determining the extent of the beam divergence, the strength of the index of refraction change can be determined. It was found that the beam divergence was smaller when focused in a modified region as compared with a beam focused in a fresh sample (Fig. 1.3). This corresponds with an increase in the beam width of a factor of five [22]. Because of the shape of the lens, the defocusing has been attributed to a decrease in refractive index which is approximately 2.5% [22]. This change in the refractive index is mostly due to the presence of the nanocracks.

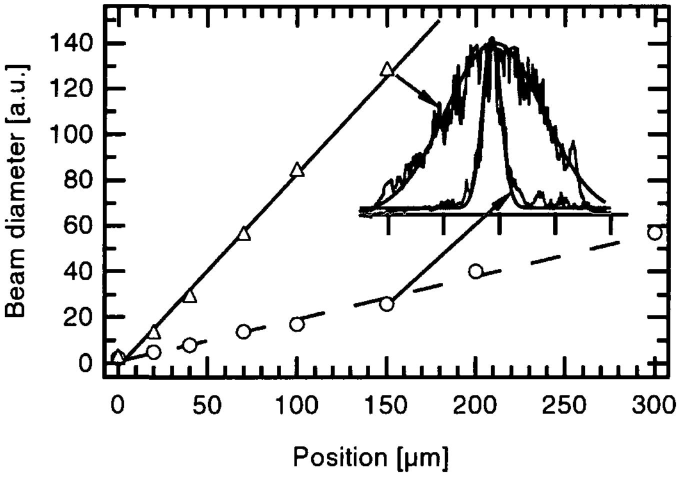

Figure 1.3: *Beam diameter as a function of distance from the focus of the laser. Red line indicates laser through unmodified region and blue line indicates laser through modified region. (from [22])*

1.2 Nonlinear Ionization Processes and Plasma Formation

The frequency of light used in these micromachining processes in dielectrics is in the infrared regime, where the energy of a single photon is not large enough to induce transitions from the valence band to the conduction band of wide band-gap materials. Therefore, femtosecond lasers induce material damage through several nonlinear ionization processes, depending on the intensity, pulse duration and material parameters. These are: multiphoton ionization (MPI), avalanche ionization and tunnel ionization. [3]

Multiphoton ionization occurs when a bound (valence) electron absorbs two or more photons simultaneously. In this process, the electron occupies virtual intermediate states between the final and initial states while the photons interact with the particle. The rate of this reaction depends on the laser intensity and the MPI cross-section. The cross-sections are very small since it is unlikely for multiple photons to interact with one electron simultaneously. However, the high intensities of femtosecond pulses allow the rates of multiphoton transitions to become appreciable [3]. For even higher laser intensities, the laser electric field is sufficiently high that its potential becomes comparable to the binding energy of the electrons. When added to the Coulomb potential of the parent atom (as felt by the bound electron), it creates a finite barrier through which the electron can tunnel to become free. This process is called tunnel ionization [7]. Free electrons can induce further ionization through a process called avalanche (or collisional) ionization. After an electron has been ionized from its parent atom, it can absorb energy from the electric field through inverse Bremsstrahlung heating. Once the electron has a kinetic energy greater than the ionization potential, the electron can inelastically collide with a bound electron causing it to become ionized. This process is important once the number of free electrons is appreciable and the pulse durations long enough for sufficient electron heating to take place [52].

Depending on the duration of the pulse, different ionization processes may dominate. For long pulses (picosecond or nanosecond durations), the intensity is not large enough to excite multiphoton ionization. Therefore the dominant process is avalanche ionization [69]. The seed electrons for this process are electrons ionized from defect locations that have lower ionization potentials. Because the defects are random, the initial number and distribution of electrons is not determinate. This creates a modified region that is not well controlled or reproducible. At durations shorter than 1 ps but larger than 10 fs, there is a combination of multiphoton ionization and avalanche ionization [52]. The seed electrons in this case are created by multiphoton ionization. Since multiphoton ionization occurs everywhere in the dielectric, this process produces uniform results that can be reproduced easily. Avalanche ionization occurs over time scales greater than 10 fs, therefore at time scales smaller this the only ionization process is multiphoton ionization [52]. Since material modification in dielectrics is typically achieved at fluences too low for significant changes to the binding potential of atoms, the cross-section for tunneling ionization is much smaller than that of multiphoton ionization and tunnel ionization does not usually play an important role [69]. It is important to note that the time scale for thermal diffusion is on the order of nanoseconds. Thus, for pulse durations less than 1 ps, there is no thermal diffusion during the pulse [20]. For small repetition rates, this allows for a more precise modified region since there is no heating of the surrounding material.

1.3 Material Modification

When a laser is focused into a dielectric, the nonlinear ionization processes discussed in Section 1.2 cause plasma formation. The region of plasma formation is thought to correspond to the material modified region because the diffusion of the electrons is small. Thus a study of the macroscopic structure of the ionization should correspond to an understanding of the material damage.

There are a few possible mechanisms that could explain how the plasma formation leads to a change in the refractive index. The ionization and subsequent recombination of the material after the laser pulse could produce colour centres (point defects in lattice structures) that modify the refractive index [62]. Another possibility is that the energy from the laser causes a melting of the focal region. This region then solidifies quickly changing the density, which causes changes in the refractive index [55]. A third possibility is that the ionization produces permanent modifications to the chemical structure of the material which cause a change in the density [11]. These three possible mechanisms probably occur in the medium concurrently; however, the relative importance of each process depends on the material of interest and the properties of the laser [69].

1.4 Current Numerical Simulations

The creation of optical systems, such as 3D waveguides, microfluidic devices and data storage devices, using nonlinear ionization in transparent dielectrics is a relatively young field. Because of the high intensities of ultrashort lasers and this new technology, there has been an increase in the number of numerical studies on nonlinear ionization in dielectrics. However, the majority of these studies have been one-dimensional and concentrated on the importance of multiphoton, tunnelling or avalanche ionization for different pulse durations [47, 51, 45, 28, 52, 72]. The next generation of simulations, which begin to look at what causes the large scale structures of the modified regions, have begun to surface in the past couple of years [53, 60, 1, 9]. However, they do not form a complete analysis of the problem.

As seen in Section 1.1, the modified region observed by experimentalists has a distinct shape (Fig. 1.2). However, it is unclear what underlying mechanisms are responsible for this shape. Numerical simulations can give insight since they give the ability to include many of the important processes as well as change the impact and value of these processes.

There are some studies that use two and three dimensional simulations to model the shape of the ionized region. Arnold et al [1] determined that the shape of the modified region depends on the numerical aperture (NA) using a three-dimensional model. For high NA, the region is confined to a smaller, circular region while for small NA, the modified region is elongated as seen in Section 1.1. Romanova et al [53] determined the temperature distribution due to multiphoton ionization. They assume the change in refractive index is due to heating of the glass and obtain the two-dimensional shape of the modified region for two different dielectrics. Burakov et al [9] use a two-dimensional nonlinear optical Schrödinger equation to analyze the ionization patterns produced by femtosecond and picosecond lasers. They attribute the elongated modified region to the nonlinear defocusing due to the plasma and Kerr effect.

While these simulations provide some insight into the shape of the region, most are not in three-dimensions and do not provide a definitive cause of the shape of the modified region. Arnold et al [1] do simulate in three-dimensions however, they only investigate the affects of numerical aperature. The two-dimensional simulations by Romanova et al [53] and Burakov et al [9] assume cylindrical symmetry and show only the final configuration of the electron density giving an incomplete picture of the dynamics of the modified region. They also include all components of the interaction making it difficult to determine the impact of each parameter and the cause of the shape of the modified region.

It has also been theorized that the Kerr effect is not important when nonlinear ionization is present. In Grojo et al [22] and Rayner et al [50], it has been proposed that this shape arises from the depletion of the incident laser beam. Since, in solids, there are orders of magnitude more ionizable molecules than photons to excite these molecules [3], the depletion of the beam becomes an important factor in the nonlinear process. They hypothesize that the intensity will not exceed the threshold intensity because, once the intensity is high enough, ionization will occur and absorb photons. The intensity profile would then appear cut at the threshold. This is referred to as self-limited absorption, or more colloquially, a "lawn-mower" effect, since the intensity is cut at a certain value. In a Gaussian beam, such as with a focused laser, as the beam width narrows and the peak intensity increases, a larger portion of the intensity curve will be cut off (Fig. 1.4). When the intensity reaches that required for multiphoton ionization near the focus, photons are absorbed until the intensity is no longer high enough for multiphoton ionization. In the laser beam, the intensity is highest in the centre. Therefore, the less intense portions of the beam farther from the centre are depleted first leaving a narrowing region of intensities large enough for nonlinear ionization. This causes the narrowing of the ionizing region. Rayner et al model this effect by simply cutting the intensity at the threshold and assuming that the energy from the photons was used to ionize the material. This gave a shape similar to that found by experiment.

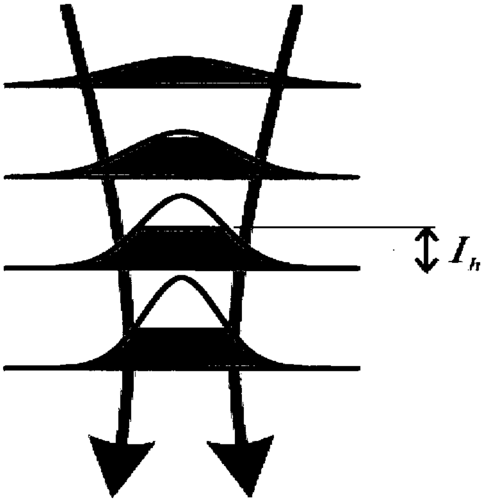

Figure 1.4: *Intensity profile cut-off at threshold as beam is focused (from [50]*

1.5 Periodic Nanocracks

In a specific range of pulse energies (approximately 150-300 nJ), periodic nanostructures have been observed in the modified region of fused silica that have been exposed to linearly polarized pulses (Fig. 1.5). These structures have dimensions smaller than the diffraction limit of light; the thickness of the planes is approximately 10 nm. The periodicity of these planes is approximately $\frac{\lambda}{2n}$ where n is the refractive index of the material and λ is the wavelength of light in a vacuum. As seen in Fig. 1.5, the orientation of the planes is perpendicular to the polarization of the electric field. These structures are not visible in crystalline solids which implies that they arise from the defects of the fused silica. It is interesting that while the defects are inherently random in distribution and size, the periodicity of the planes does not change from experiment to experiment.

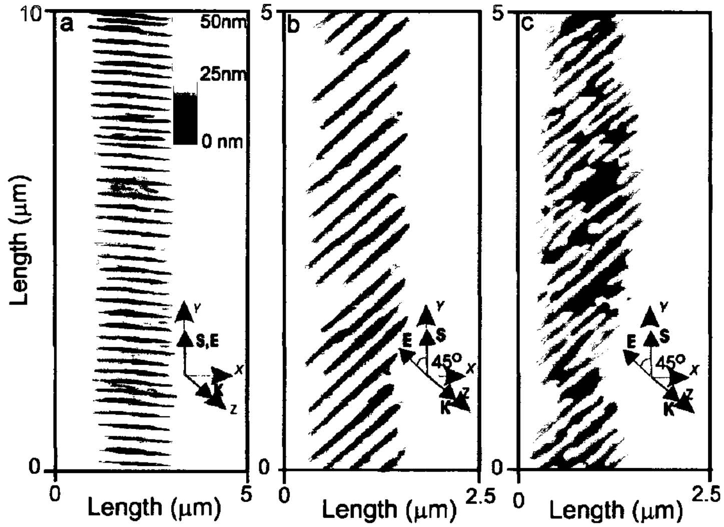

Figure 1.5: *Modified region with periodic nanocracks. Slice perpendicular from laser propagation direction for translated sample. The polarization of the electric field is rotated and indicated on each picture. (from [4])*

There are two competing theories which explain the periodic nanocracks. One suggests that there is an interference effect between the electric field produced by the laser and the oscillations of the plasma formed from nonlinear ionization. Another theory suggests that impurities are ionized first creating nanoplasmas. These nanoplasmas grow preferentially in the direction of propagation of the light creating nanoplanes. The organization of the nanoplanes into periodic nanocracks is due to modes similar to those found in metallic waveguides which have enhancements in the electric field along nanoplanes with a spacing of $\frac{\lambda}{2n}$. Both of these are now described in greater detail in the following subsections.

1.5.1 Bulk Plasma Oscillation Theory

Shimotsuma et al [58] argue that the structures are a result of the interference of plasma oscillations and the laser field. Once there is an appreciable electron density, the charged particles will behave as a plasma. The plasma will gain energy through inverse Bremsstrahlung heating which will cause bulk electron density waves. These waves oscillate parallel to the electric field created by their moving charge. They can couple to the laser field if the polarization of the laser field is in the same direction as the electric field created by the plasma waves. The initial coupling is due to inhomogeneities in the electron motion. As an interference pattern develops between the plasma waves and the laser field, the coupling is reinforced creating a positive feedback loop between the interference pattern and the coupling. The electrons will be preferentially located along the constructive regions of high electric field. When the material recombines, this uneven distribution of electrons will create nanocracks.

In order to efficiently create the interference pattern, momentum and energy must be conserved. This gives a relationship between the wave number of the grating period, the laser field and the plasma oscillations.

$$k_{gr} = \frac{2\pi}{\Lambda} = \sqrt{k_{pl}^2 - k_{ph}^2} \tag{1.1}$$

where Λ is the grating period, k_{pl} is the wave number of the plasma and k_{ph} is the wave number of the laser field. The momentum of the plasma is given by

$$k_{pl} = \frac{\omega_{pl}}{\nu_{pl}} \tag{1.2}$$

where ω_{pl} is the angular frequency of the plasma and ν_{pl} is the speed.

Using the dispersion relation for electron plasma waves (Langmuir waves), they find

$$\omega_{pl}^2 = \omega_p^2 + \frac{3}{2}\nu_e^2 k_{pl}^2 \tag{1.3}$$

Conservation of energy implies that $\omega_{pl} = \omega$. Combining this relation with 1.1 and 1.3, $\omega_p = \sqrt{\frac{N_e e^2}{\epsilon_0 m_e}}$ and $\nu_e = \sqrt{\frac{2k_B T_e}{m_e}}$ they find an equation for the grating period in terms of electron temperature and density.

$$\Lambda = \frac{2\pi}{\sqrt{\frac{1}{T_e}\left(\frac{m_e\omega^2}{3k_B} - \frac{e^2 N_e}{3\epsilon_0 k_B}\right) - k_{ph}^2}} \tag{1.4}$$

where N_e is the electron density, k_B is the Boltzmann constant, m_e is the electron mass, e is the electron charge and T_e is the electron temperature (Fig. 1.6).

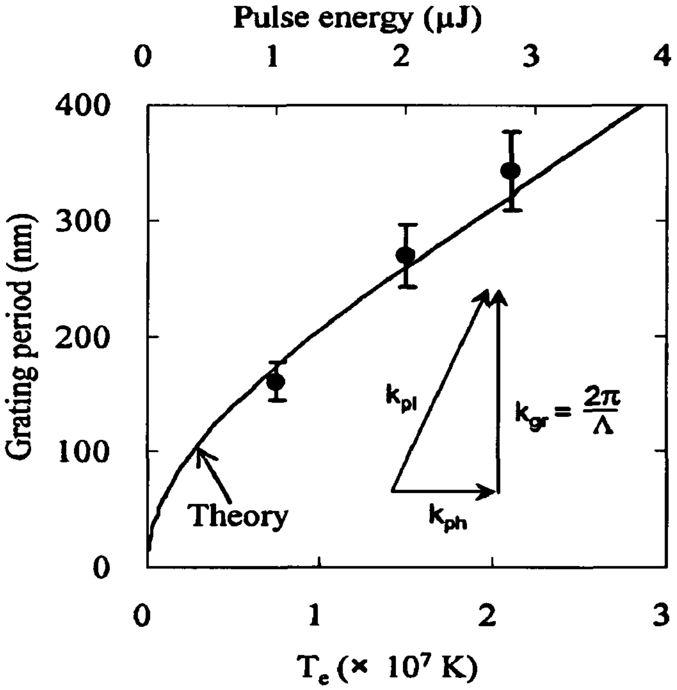

Figure 1.6: *The line represents theoretical grating periods as a function of temperature. Data points represent experimental grating periods as a function of pulse energy. (from [58])*

Another theory that Kazansky et al [30] introduced is that the structures are created by the interference of two bulk plasmons with approximately half the energy of the light. This model was adopted because it produced more realistic electron energies and electron densities than the theory described above. The energy conservation condition gives a dispersion relation of $\omega = \omega_{pl}^{(1)} + \omega_{pl}^{(2)} = \omega_{pl} + \omega_p$ where $\omega_{pl}^{(1)}$ and $\omega_{pl}^{(2)}$ are the angular frequencies of the two bulk plasma oscillations. Following a similar procedure as in the previous model, they arrive at a spacing period for the structures.

$$\Lambda = \frac{\lambda}{2c\sqrt{\frac{1}{3\nu_e^2}\left(1 - 2\frac{\omega_p}{\omega}\right) - \frac{n^2}{c^2}\left(1 - \frac{\omega_p}{\omega}\right)}} \tag{1.5}$$

While this model explains the periodicity of the structures it does not provide a definitive explanation of these structures. The spacing of the nanocracks given by this model is a function of the laser pulse energy. Bhardwaj et al [3] found that the spacing is independent of pulse energy and $\Lambda = \frac{\lambda}{2n}$ where λ is the central wavelength of the laser field and n is the refractive index of the material. This model does not, in general, give this spacing. As well, this model fails to explain the decrease in grating period with an increase in number of shots [14]. As of yet, more research is required to confirm or reject this model.

1.5.2 Nanoplasma Theory

Rajeev et al [48] present a different theory for the creation of these nanocracks. They argue that local defects, such as colour centres and impurity sites, and thermal noise in a dielectric lower the ionization potential of certain electrons. Once these electrons are ionized, they assist in the ionization of other molecules in the region surrounding by enhancing the Coulomb field [19]. These processes result in localized hot spots.

As noted in Section 1.1, when a dielectric has been previously ionized, the ionization potential will decrease for subsequent laser pulses. Since, in a solid, the ionized electrons cannot leave the region where they are initially created, the effects of this memory are local. As a result, over subsequent laser pulses, the initially ionized hot spots would grow into spherical nanoplasmas.

The properties of the nanoplasmas will depend on their electron density. If the density of a plasma reaches the critical density, light can no longer propagate in the plasma and it is said to be overdense. In this case the plasma behaves like a metal. In the case where the plasma density is lower than the critical density, the plasma is said to be underdense.

In either case, the nanoplasmas are polarizable, and create local field effects that are caused by oscillating dipole charges induced by the laser field. At a specific instant in time, the local field effects can be determined by solving Laplace's equation. For a spheroid with dielectric constant $\epsilon_r + i\epsilon_i$ in a medium of dielectric constant ϵ_d, the local field effects have been determined analytically [5]. Rajeev et al [48] take a spheroid with a polar length of a and an equatorial length of b in a plane wave electric field, oriented such that the pole is parallel with the electric field vector and perpendicular to the propagation (Fig. 1.7). The electric fields at the pole and equator can be given in terms of the incident electric field.

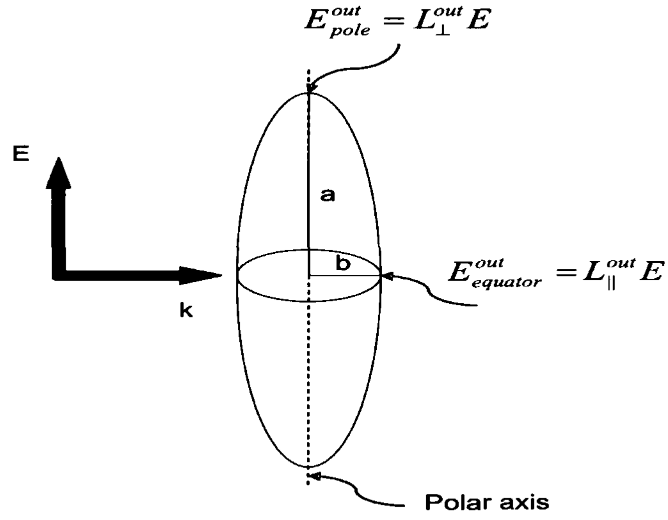

Figure 1.7: *Plasma spheroid in Electric field. The local fields are indicated at the poles and equator. Electric field and propagation are defined (from [48])*

$$E^{out}_{pole} = \frac{f(\frac{a}{b})}{\epsilon - 1 + f(\frac{a}{b})} E \tag{1.6}$$

$$E^{out}_{equator} = \frac{f(\frac{a}{b})}{\epsilon(\epsilon - 1 + f(\frac{a}{b}))} E \tag{1.7}$$

where $\epsilon = \frac{\epsilon_r}{\epsilon_d}$.

For a spherical plasma, $\frac{a}{b} = 1$ and $f(\frac{a}{b}) = 3$. Therefore, equations 1.6 and 1.7 become

$$E^{out}_{pole} = \frac{3\epsilon E}{\epsilon + 2} \tag{1.8}$$

$$E^{out}_{equator} = \frac{3E}{\epsilon + 2} \tag{1.9}$$

For a metal, $\epsilon \ll -2$ which gives the relation $E^{out}_{pole} > E$. The parallel component of the electric field must be continuous across the boundary. Inside a metal, the electric field must be zero. Since the electric field is parallel to the equator of the sphere, $E^{out}_{equator} = 0$. The field is therefore enhanced along the pole of the sphere. In the case of an underdense plasma, $0 < \epsilon < 1$. This gives $E^{out}_{equator} > E^{out}_{pole}$; an enhancement along the equatorial plane of the sphere. Because of the highly nonlinear dependence on intensity of the ionization process, the field enhancements are hypothesized to drive the growth of the nanoplasma along the equatorial plane. For an underdense plasma, the field enhancements are approximately independent of the ratio of $\frac{a}{b}$ [48]. Thus, as the nanoplasma grows, the field enhancements would encourage the growth. These nanoplasmas could then grow into nanoplanes (Fig. 1.8). Rajeev et al [48] suggest that the orientation of the observed nanocracks with respect to the laser polarization indicates that for the majority of the laser pulse, these nanoplasmas will be underdense. At the final stages of the pulse, the nanoplasmas may become overdense. However, they assume that the centres of the nanoplasmas would become overdense and a gradation will exist. Thus the outer regions of the nanoplasmas will behave as if they were underdense.

Rajeev et al [48] predict that each nanoplane would then grow from a nanoplasma. Since the nanoplasmas are seeded by randomly located defects, these nanoplanes would have a random arrangement. Throughout the subsequent pulses, these nanoplanes develop a higher electron density, particularly in the centre. This gives them a semi-metallic structure: along the edges that influence the local field effects, the decreasing density causes them to behave as an underdense plasma, near the centre, the high density core causes them to behave as thin metallic planes. These metallic properties could then influence the propagation of light.

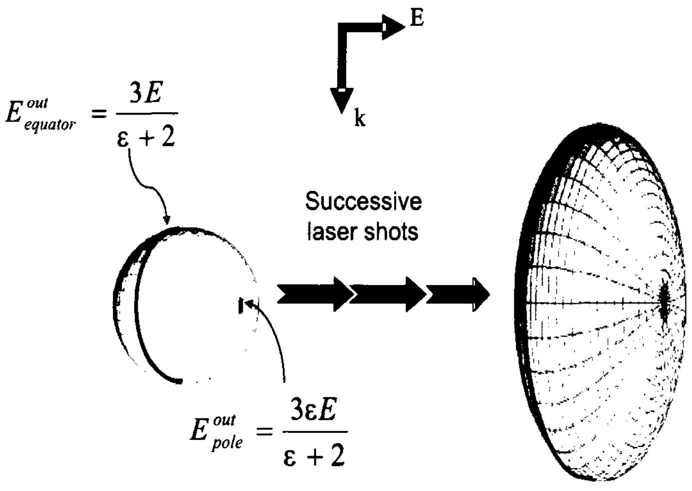

Figure 1.8: *Nanospheres grow into nanoplanes (from [48])*

Since the nanoplanes have metallic properties, it is predicted that they can act as metallic waveguides (Section 2.1). In a parallel plate waveguide, the electromagnetic field has a characteristic profile. If the profile of the field has an increased intensity along the plasmas, this would cause preferential growth of the nanoplanes at certain spacings.

There are two possible polarizations for metallic waveguides: the transverse electric (TE) and the transverse magnetic (TM). The TE modes have non-zero component of the electric field in the transverse direction while the TM modes have a non-zero transverse component of the magnetic field. The field profiles of these modes are well known and the first mode is depicted in Fig. 1.9 [48]. The fields show a sinusoidal profile with a period equal to twice the spacing of the metals.

Along the surfaces of the nanoplanes, it is postulated that surface plasmon polaritons can be excited. These are plasma oscillations which are confined to the interface between the plasma and the dielectric. The surface plasmons would be coupled to the incident light through random surface roughness along the nanoplanes. For a TE mode, the fields can only satisfy the boundary conditions across the metal/dielectric interface if they are zero, and so surface plasmon polaritons are inherently TM modes. Therefore Rajeev et al [48] predict that the

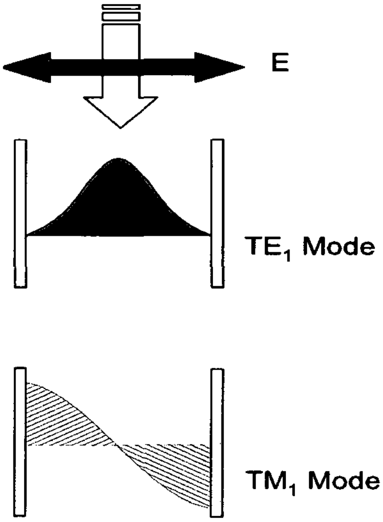

Figure 1.9: *Electric field and Magnetic fields from* TE_1 *and* TM_1 *Modes, respectively (from [48])*

waveguides will be preferentially excited in TM modes.

According to Rajeev et al [48], in the TM case, the electric field is enhanced at the interface. This will encourage growth of the nanoplanes that are a distance of half the wavelength of light from each other creating a periodic distribution of these charged nanoplanes. Once the material is left to recombine, the areas that have been ionized, the nanoplanes, will have a modified index of refraction. This creates the periodic structures that are seen in the material.

1.6 Thesis Organization and Contributions

The femtosecond laser-induced dielectric modification process is still not well understood. To the best of our knowledge, this subject has mostly been researched experimentally. It is not certain which processes are important for determining the characteristic carrot shape of the modified region. The shape has been attributed to the balance between plasma dispersion and self-focusing as well as the self-limiting absorption caused by multiphoton absorption. In addition, the theories that have been mentioned in Sections 1.5.1 and 1.5.2 that attempt to describe nanocrack formation have yet to be rigorously studied theoretically. In this thesis, I will examine several aspects of the material modification process, using both analytical and computational techinques.

Using analytical techniques, I will investigate the organization of the planes. In the theory of nanocrack formation presented by Rajeev et al [48] (Section 1.5.2), the nanoplanes are assumed to behave as metallic planes in order to explain the nanocrack separation, but at the same time have underdense outer portion to maintain preferential growth into nanocracks perpendicular to the laser polarization. In Chapter 2, I thoroughly investigate the mode structure for metallic waveguides and apply the results to the model introduced by Rajeev et al [48]. I then use an analytical formalism to calculate the modes of planes that are not necessarily metallic, but for plasmas that have a finite plasma frequency (ω_p), which would be the more realistic scenario. In particular, I calculate the transverse magnetic modes of a plasma waveguide with a variable plasma frequency. As well, I use the mode structure and propagation constant to find the minimum spacing of the nanocracks. I find that this minimum spacing decreases with decreasing plasma frequency.

In Chapter 3, I use a standard method for solving Maxwell's equations in the time domain, the Finite-Difference Time-Domain algorithm and extend it by including nonlinear processes and the dynamic build up of the electron plasma. The functions added to this code include implementations for the Drude model for a dispersive medium, multiphoton and avalanche ionization and the Kerr nonlinearity. As well, the electromagnetic sources were extended to include a focused Gaussian beam, an angled plane wave, ellipitically and circularly polarized light. This code is quite versitile. It calculates the $\vec{E}$ and $\vec{H}$ fields and the electron density for each point in space and time. Thus we can observe a progression of the fields and electron density in time. The medium can easily be changed by changing various paramaters in an input file. The electron density and index of refraction can be initialized in almost any pattern allowing many different materials and geometries to be simulated.

A large part of this thesis work was the development of this code. In Chapter 4, I use this code for one set of simulations, where a Gaussian laser pulse focused inside a nonlinear dielectric which emulates the experiments that create the modified region discussed in this chapter. The ionized area produced in the simulation closely resembles that observed by experiment. We were able to verify the existence of a self-limited absorption (or lawn-mower) effect on a Gaussian pulse in time. It was also found that the region is not cylindrically symmetric. Rather, when viewed in cross-section, it is elongated along the direction parallel to the polarization of the light. While observing the formation of the modified region as a function of time, we found that transient periodic ridges perpendicular to the propagation direction of light are formed (not the same direction as the periodic nanocracks discussed above). They have a spacing of $\lambda/2n$ and are suspected to arise from a sub-cycle lawnmower affect. They appear to smear out by the end of the laser pulse. Finally, and most importantly, we find that multiphoton absorption is the main cause of the distinct shape of the damaged area. Although the plasma dispersion and self-focusing create larger electron densities and, in the case of self-focusing, a shift in the location of the electron density peak, they do not affect the general shape. We were able to determine the time and intensity dependence of this area as well as the effects of self-focusing, plasma dispersion and multiphoton absorption on the formation of the modified region.

Chapter 2

Analytic Analysis: Spacing of the Nano-planes

As discussed in Section 1.5.2, Rajeev et al [48] argue that the ordering of the periodic nanoplanes is caused by the interaction of incident light with randomly positioned nanoplanes of plasma. They hypothesize that the randomly distributed nanoplanes behave like metallic waveguides creating an increased field at the surface of those that have a spacing of $\frac{\lambda}{2n}$ or greater from adjacent nanoplanes. This increased field would then encourage the growth of these pairs of nanoplanes creating the structures seen in experiments.

Since this argument was posed, new experiments have showed that the spacing between the cracks can be smaller than $\frac{\lambda}{2n}$ [14]. This would appear to weaken this theory. However, the theory makes the assumption that the plasma acts as a perfect conductor while in reality the plasma properties are determined by the plasma frequency, which is unknown. This chapter will explore the change to electric field profile and the minimum spacing of the cracks if the plasma frequency is taken to be finite, and the plasma dielectric response is modeled by the Drude model.

For the multilayer parallel plate waveguide derivations we outline below, a propagation constant is defined as the wave number in the direction of propagation (in our case, the z-

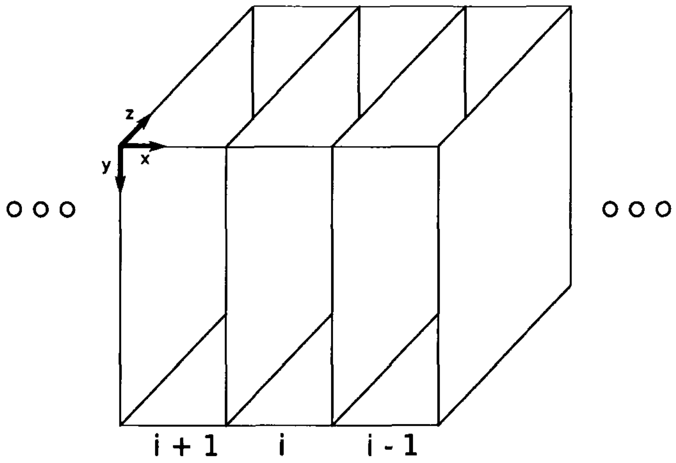

Figure 2.1: *Infinite parallel plate waveguide*

direction as seen in Fig. 2.1). In order for a mode to propagate in a waveguide, the propagation constant must have a real component. This puts a limit on the spacing of the parallel plates for which propagating modes exist. According to Rajeev et al [48], the minimum spacing corresponds to the spacing of the nanoplanes.

2.1 Waveguides

We begin with the general theory of propagating modes in parallel plate waveguides [13]. A parallel plate waveguide consists of layers of different materials. The electric and magnetic fields in the dielectric layer i with index of refraction n_i are given by Maxwell's equations for the electric field $\vec{E}$ and magnetic field $\vec{H}$:

$$\nabla \times \vec{H} = \frac{n_i^2}{c}\frac{\partial \vec{E}}{\partial t} \tag{2.1}$$

$$\nabla \times \vec{E} = -\frac{1}{c}\frac{\partial \vec{H}}{\partial t} \tag{2.2}$$

We consider time harmonic fields that are propagating in the z-direction. This gives fields of the form

$$\vec{H} = \vec{H}_0(x, y)e^{I(\omega t - \beta z)} \tag{2.3}$$

$$\vec{E} = \vec{E}_0(x, y)e^{I(\omega t - \beta z)} \tag{2.4}$$

where β is the propagation constant, ω is the angular frequency of the light and $I = \sqrt{-1}$. For propagating solutions, β must have a real component.

In the case of a parallel plate waveguide, the index of refraction varies in the x-direction and is uniform in the y-direction. Therefore, we can assume that $\vec{H}_0$ and $\vec{E}_0$ depend only on x. Thus,

$$\frac{\partial \vec{E}_0}{\partial y} = \frac{\partial \vec{H}_0}{\partial y} = 0. \tag{2.5}$$

Substituting 2.3 and 2.4 into 2.1 and 2.2 and dividing by $e^{I(\omega t - \beta z)}$, we get two sets of equations that are indpendent of each other. Equations involving only E_y, H_x and H_z are:

$$-I\beta H_x - \frac{\partial H_z}{\partial x} = \frac{I\omega n_i^2}{c}E_y \tag{2.6}$$

$$I\beta E_y = -\frac{I\omega}{c}H_x \tag{2.7}$$

$$\frac{\partial E_y}{\partial x} = -\frac{I\omega}{c}H_z \tag{2.8}$$

Equations only involving H_y, E_x and E_z are:

$$I\beta H_y = \frac{I\omega n_i^2}{c}E_x \tag{2.9}$$

$$\frac{\partial H_y}{\partial x} = \frac{I\omega n_i^2}{c}E_z \tag{2.10}$$

$$I\beta E_x + \frac{\partial E_z}{\partial x} = \frac{I\omega}{c}H_y \tag{2.11}$$

When there is no component of the electric field in the direction of propagation, the mode is called transverse electric (TE) (Eq. 2.6, 2.7, 2.8). When there is no component of the magnetic field in the direction of propagation, the mode is called transverse magnetic (TM) (Eq. 2.9, 2.10, 2.11). There is also one transverse electromagnetic mode (TEM) which contains all fields.

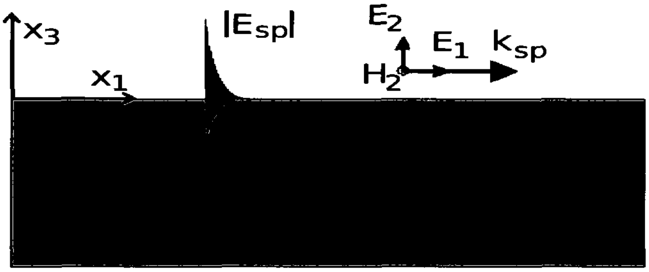

Figure 2.2: *Surface plasmon polariton at a dielectric/metal interface (from [74])*

In Rajeev et al [48], it is hypothesized that surface roughness couples with the incident light to create surface plasmon polaritons (SPP). These are plasma oscillations which are confined to a dielectric/metal interface (Fig. 2.2). The field from these oscillations propagates along the surface and decays exponentially in the directions perpendicular to the surface. These conditions, along with conservation of momentum, cause the fields for TE modes, including the TEM mode, to vanish. As the light is assumed to be coupled to the SPPs, the light will propagate in TM modes and so we focus on the TM modes in what follows.

Combining equations 2.9, 2.10 and 2.11 gives

$$\frac{\partial^2 H_y}{\partial x^2} + \alpha_i^2 H_y = 0 \tag{2.12}$$

where

$$\alpha_i = (k^2 n_i^2 - \beta^2)^{\frac{1}{2}} \tag{2.13}$$

$$k = \frac{\omega}{c} = \frac{2\pi}{\lambda} \tag{2.14}$$

and n_i is the index of refraction for the i^{th} medium. From this equation, we find that the solution of H_y is

$$H_y = A_i e^{\alpha_i x} + B_i e^{-\alpha_i x} \tag{2.15}$$

where A_i and B_i are constants which must be determined. If $k^2 n_i^2 - \beta^2 < 0$, α_i becomes imaginary. This implies that the solutions are sinusoidal in the x-direction. If $k^2 n_i^2 - \beta^2 \geq 0$, α_i is real and the solutions are exponentially decaying or growing. For bound modes, the fields in the outer layers must be exponentially decaying. Therefore, if α_0 and α_2 are real we choose $B_0 = A_2 = 0$.

Along the boundary of two materials, for the TM modes, E_z is continuous. By Eq. 2.10, the continuity of E_z implies that $\frac{1}{n_i^2}\frac{\partial H_y}{\partial x}$ is continuous. To complete this problem, we need to apply the boundary conditions for E_z and H_y to all interfaces to create a set of equations for A_i and B_i. This set of equations must have a solution, therefore, the determinant of the matrix consisting of the coefficients for A_i and B_i must be zero. Using this condition, β^2 can be determined. We do this below for two cases: 1) a set of parallel metallic waveguides separated by a dielectric, repeating the analysis of Rajeev et al [48], and 2) a set of parallel plasmonic waveguides separated by a dielectric, for arbitrary plasma frequency.

2.2 Metallic Waveguides

In the special case of a three layer waveguide with a perfect conductor for the layers $i = 0$ and $i = 2$, the electric field inside the metal is fixed at zero. Therefore,

$$E_z(0) = 0 \tag{2.16}$$

$$E_z(d) = 0 \tag{2.17}$$

In a perfect conductor, the index of refraction is not defined. Therefore, we cannot evaluate the continuity in terms of the H_y field. Thus, we will derive an equation for E_z similar to Eq.

2.12. We obtain

$$\frac{\partial^2 E_z}{\partial x^2} + \alpha^2 E_z = 0 \tag{2.18}$$

From Eq. 2.18, we determine

$$E_z = A_n sin(\alpha x) \tag{2.19}$$

where we define $\alpha = \frac{m\pi}{d}$, m is any integer and d is the spacing of the metallic plates so that the electric field is zero at the interfaces. Substituting Eq. 2.19 into Eq. 2.9 - 2.11, we find the value of the remaining components

$$E_x = \frac{\beta}{\alpha} A_n cos(\alpha x) \tag{2.20}$$

$$H_y = \frac{In\omega}{\alpha c} A_n cos(\alpha x) \tag{2.21}$$

From Eq. 2.13, we find the propagation constant to be

$$\beta^2 = n^2 (\frac{2\pi}{\lambda})^2 - (\frac{m\pi}{d})^2 \tag{2.22}$$

where we have substituted $k = \frac{2\pi}{\lambda}$.

In order for the waves to have propagating solutions, β must be real. This implies that β^2 must be greater than zero. There is one solution of $\beta^2 = 0$ for each value of m. This can be seen in a plot of waveguide spacing (*d*) versus β^2 (Fig 2.3). When $m = 1$, the first TM mode, the minimum spacing of the waveguides is $\frac{\lambda}{2n}$. At this spacing, there is a peak in the H_y field at the surface of the waveguide, but also a peak in E_z in between the interfaces. Thus it is not entirely clear what the effect this would have on nonlinear ionization, which was postulated to be enhanced at the interfaces.

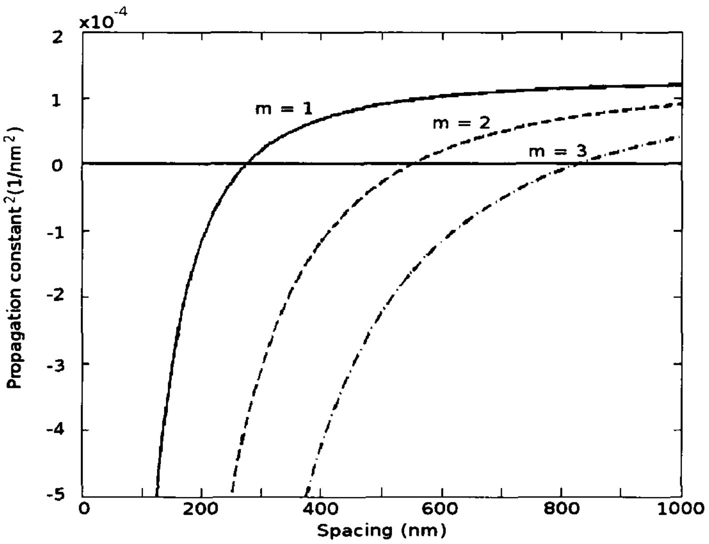

Figure 2.3: *Minimum spacing for propagating modes plotted against propagation constant^2 (β^2) for a perfect conductor waveguide.*

2.3 Plasma Waveguide

In reality, the nanoplanes are not perfectly conducting metals but are plasmas with a finite plasma frequency (ω_p). We model the dielectric response of the plasma with the Drude model. Therefore we set

$$n_0 = n_2 = \sqrt{1 - \frac{\omega_p^2}{\omega(\omega - I\Gamma)}} \tag{2.23}$$

where n_0 and n_2 are the indices of refraction in the plasma and Γ is the response time of the plasma. We use this to substitute n_0 and n_2 into Eq. 2.13 for α_0 and α_2. The nanoplanes are assumed to be overdense since the field must decay inside the plasma for confined modes for this configuration. Since the index of refraction is complex, the propagation constant will always be complex. However, if there is a real part of the propagation constant, there will still be propagating solutions.

Applying the boundary conditions, we find

$$M\begin{bmatrix} A_0 \\ A_1 \\ B_1 \\ B_2 \end{bmatrix} = \begin{bmatrix} 1 & 1 & 1 & 0 \\ 0 & e^{-\alpha_1 d} & e^{\alpha_1 d} & e^{-\alpha_2 d} \\ \frac{\alpha_0}{n_0^2} & -\frac{\alpha_1}{n_1^2} & \frac{\alpha_1}{n_1^2} & 0 \\ 0 & -\frac{\alpha_1 e^{-\alpha_1 d}}{n_1^2} & \frac{\alpha_1 e^{\alpha_1 d}}{n_1^2} & \frac{\alpha_2 e^{-\alpha_2 d}}{n_2^2} \end{bmatrix} \begin{bmatrix} A_0 \\ A_1 \\ B_1 \\ B_2 \end{bmatrix} = 0$$

For non-trivial solutions to exist, $det(M) = 0$. Substituting equation 2.23 into matrix M and taking the determinant, we find

$$\frac{n_2^2}{\delta}(\frac{2\delta}{n_2^2}cos\alpha d + \frac{n_1^2}{\alpha}(\frac{\delta^2}{n_2^4} - \frac{\alpha^2}{n_1^4})sin\alpha a) = 0 \tag{2.24}$$

where we have defined the following quantities

$$\begin{aligned} \delta &= \sqrt{\beta^2 - k_p^2} \\ \alpha &= \sqrt{k_1^2 - \beta^2} \\ k_p &= \sqrt{1 - \tfrac{\omega_p^2}{\omega(\omega - I\Gamma)}}\,\tfrac{2\pi}{\lambda} \\ k_1 &= \tfrac{2\pi n_1}{\lambda} \end{aligned}$$

To determine the propagation constant, Eq. 2.24 must be solved numerically. Since β^2 is complex, it is substituted by $\beta^2 = Re(\beta^2) + I\,(Im(\beta^2))$. The equation is then split into real and imaginary parts. We now have two equations (the real and imaginary parts of Eq. 2.24) and two unknowns ($Re(\beta^2)$ and $Im(\beta^2)$).

This system of equations was solved with a Matlab function that determines the roots of a function near a given initial value using the trust-region-dogleg method. To create a plot similar to Fig. 2.3, all of the roots at each spacing were needed. These were determined, for each spacing, by iterating the initial value over a region near $\beta^2 = 0$. Plots of the real and imaginary parts of β^2 are shown in Fig. 2.4.

Comparing the plot of $Re(\beta^2)$ with the metallic waveguide case (Fig. 2.3), we can see numerous modes with similar shapes to that of the metallic case. The first mode that follows

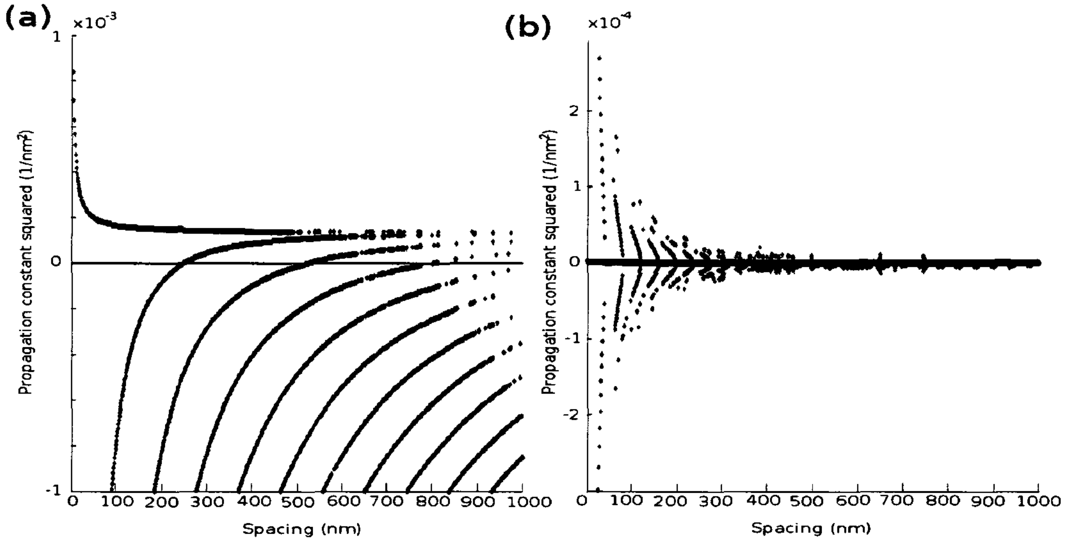

Figure 2.4: *(a) Real and (b) imaginary parts of the propagation constant squared where* $\omega_p = 10\omega$ *and* $\Gamma = 0.001\omega$. *The horizontal line in (a) indicates* $\beta^2 = 0$.

$\beta^2 = 2 \times 10^{-4} 1/nm^2$ corresponds to the TEM mode in the perfect conductor case. This mode would not be relevant to the theory considered here because surface plasmons couple only to TM modes. The first mode that crosses $\beta^2 = 0$ corresponds to the $m = 1$ mode in the perfect conductor case. This mode is taken into account when determining the minimum spacing. From these plots, it can be seen that $Re(\beta^2)$ is more than an order of magnitude larger than $Im(\beta^2)$ for all spacing except those smaller than 50 nm. Since the imaginary part of β^2 is small, there will be a large decrease in the propagation distance of the modes when the real part of β^2 becomes negative. Therefore, the minimum spacing for propagating modes can be determined as before: when $Re(\beta^2)$ is larger than zero. Once the parameter Γ is below 0.1ω, large changes do not affect the minimum spacing within our accuracy. Therefore, $\Gamma = 0.001\omega$ was used in the calculations.

To determine the minimum spacing, plots similar to Fig. 2.4 were plotted for different plasma frequencies and the spacing corresponding to the first root of $\beta^2 = 0$ was taken as the minimum spacing. We found that the spacing depends on the plasma frequency. As seen in Fig. 2.5, the minimum spacing increases for increasing ω_p, approaching that of the perfectly

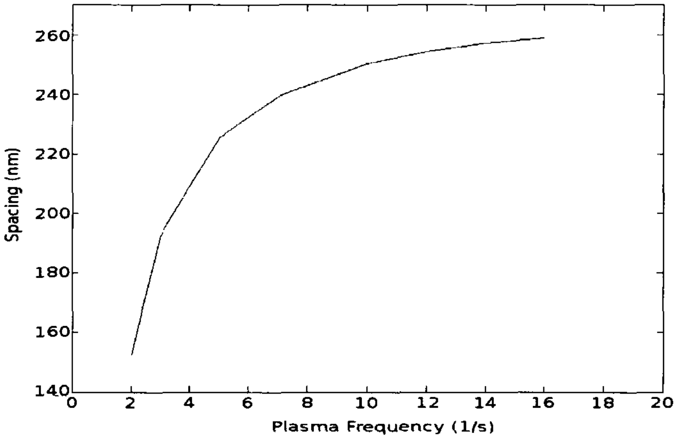

Figure 2.5: *Spacing as a function of plasma frequency*

conducting metallic waveguide case ($\frac{\lambda}{2n}$) as ω_p becomes very large. It is interesting to note that for small plasma frequencies, the spacing is less than what is expected by the perfect conducting waveguides model. This coincides with recent experimental results which indicate that the spacing can be smaller than $\frac{\lambda}{2n}$ [14]. Fig. 2.5 would also imply that there was some relationship between the intensity and duration of the laser pulse with the spacing.

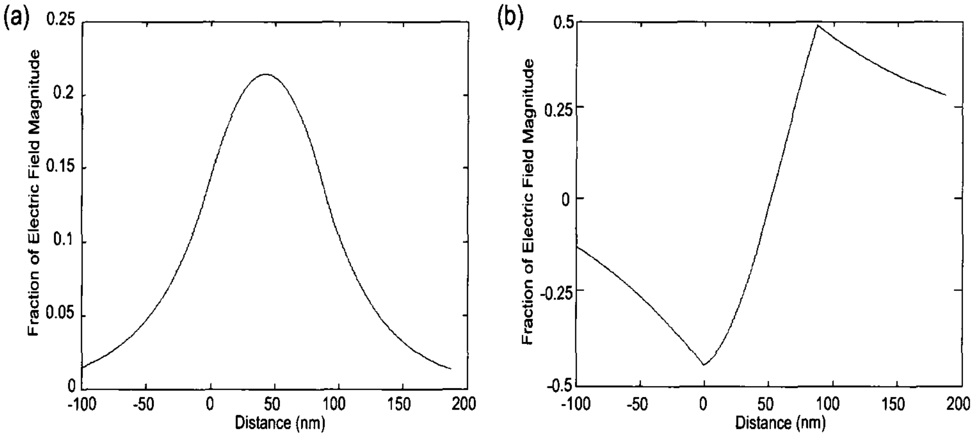

Figure 2.6: *(a) Profile of E_z component and (b) profile of H_y component in a plasma waveguide.*

We substituted the values of β and the spacing into the equation $det(M) = 0$ to determine the fields. The H_y and E_z field profiles are shown in Fig. 2.6 for a spacing of $d = 100nm$.

They are both similar to those of a perfect conductor. The electric field in this case takes on a minimum, but non-zero value at the boundaries.

Chapter 3

Numerical Methods: Finite-Difference Time-Domain

In order to understand the details of the interaction of an intense, pulsed laser with a dielectric, we need to turn to numerical simulations. Since the intensity of the laser is quite large, the nonlinear properties of the dielectric must be taken into account. Therefore, to simulate this interaction, a computational model of the dynamical development of the electron plasma due to nonlinear ionization and the effect of both nonlinear dielectric properties and the electron plasma on the light propagation needs to be implemented. In this chapter, we introduce a three-dimensional Finite-Difference Time-Domain (FDTD) approach to this problem. This approach is the first to give insight into the three-dimensional characteristics of the modified region discussed in Chapter 1. These results are discussed in Chapter 4.

Developed in 1966 by Kane Yee, the FDTD algorithm is one of the primary bruteforce methods for calculating electrodynamics on a grid. Many materials can be modeled using this method because the properties of the material can be assigned to each cell. Therefore, the interaction of light with spatially complex structures can be simulated as long as the cell size is small enough to allow for good resolution. Since all of the fields are calculated at each time step, a large amount of information is available from each simulation such as the time development and frequency dependence. The method is easily parallelized and exhibits good scaling with number of processors. However, the large computational domains necessary for most simulations require large amounts of memory and computational time. This requires efficient use of the computer's resources through optimization of the code.

In the FDTD method, the volume of interest is divided into an FDTD grid or mesh made up of individual cells of specified volume. In each cell, the electric and magnetic fields are calculated at each time step using Maxwell's equations. The time is then incremented and the fields are calculated for the entire grid using the values at the previous time step. The method calculates the fields using the central difference approximation for the time and space partial derivatives in Maxwell's equations.

The equations used to calculate the fields in the FDTD method (in cgs units) are

$$\frac{\partial \vec{D}(\vec{r},t)}{\partial t} = c\nabla \times \vec{H}(\vec{r},t) \tag{3.1}$$

$$\vec{D}(\vec{r},t) = \epsilon_r \vec{E}(\vec{r},t) + 4\pi \vec{P}(\vec{r},t) \tag{3.2}$$

$$\frac{\partial \vec{H}(\vec{r},t)}{\partial t} = -c\nabla \times \vec{E}(\vec{r},t) \tag{3.3}$$

For the purposes of this thesis, the electric current density $(\vec{J})$ and magnetic current density $(\vec{M})$ are assumed to be zero.

All of the properties of the material appear only in Eq. 3.2. Separating out the material properties from the curl equations allows for a more straightforward implementation of different materials. To implement a particular material, we need only a model for the polarization P, which can, in general, include both dispersive and nonlinear terms and do not need to modify Eq. 3.1 and Eq. 3.3.

For this thesis, an existing in-house FDTD code was expanded to analyze non-linear processes in dielectrics. The in-house code contained the basic FDTD update algorithm shown in Eq. 3.1, Eq. 3.2 and Eq. 3.3, with $\vec{P} = 0$ allowing only linear, non-dispersive media to be modeled. As well, it contained routines for a plane wave source and periodic, total field/scatter field and perfectly matched layer boundary conditions, but only for for propagation parallel to one of the axes. It was also parallelized in the x- and y-directions. This allowed the code to simulate a plane wave propagating through a linear dielectric system.

The contributions of this thesis include developing and implementing algorithms to incorporate a frequency-dependent polarization (Drude model) and nonlinear polarization components, such as the Kerr effect and multiphoton absorption. As well, Gaussian sources and different polarizations of incident light were implemented. The total-field/scatter-field boundary condition was improved to include plane wave sources propagating at an arbitrary angle. Finally, a secondary differential equation describing dynamic plasma generation through nonlinear ionization was introduced and coupled with the Maxwell's equations.

In this chapter, we describe the details of the extensions to the FDTD code, as well as a few of the pre-existing features for completeness. In Section 3.1, the fundamental equations and theory of the FDTD code are introduced. As well, we discuss the restrictions for numerical stability. In Section 3.2, the different electromagentic sources are discussed. These include plane waves, Gaussian beams and Gaussian envelopes in time, as well as different light polarizations. In Section 3.3 we discuss various boundary conditions including periodic, total field/scatter field and perfectly matched layer. Finally, in Section 3.4, we discuss the polarization ($\vec{P}$) and the non-linear ionization equation.

3.1 Basic FDTD Algorithm

To solve Maxwell's equations (Eq. 3.1 and Eq. 3.3) numerically, we will use the central difference approximation for the time and space derivatives. The most accurate implementation requires that the numerical updates for the $\vec{E}$ and $\vec{H}$ fields are staggered in time and their components are staggered in space. The electric field is calculated at time step $t = n\Delta t$ and the magnetic field is calculated at time step $t = (n + \frac{1}{2})\Delta t$, where n is an integer representing the n^{th} time step. For the spatial components, the $\vec{D}$ and $\vec{E}$ field components are located in the centre of the faces of the cell while the $\vec{H}$ field components are located at the midpoints of the edges. Each component of every field is located on a different edge or face than the others in a configuration referred to as the Yee cell; this is illustrated in Figure 3.1.

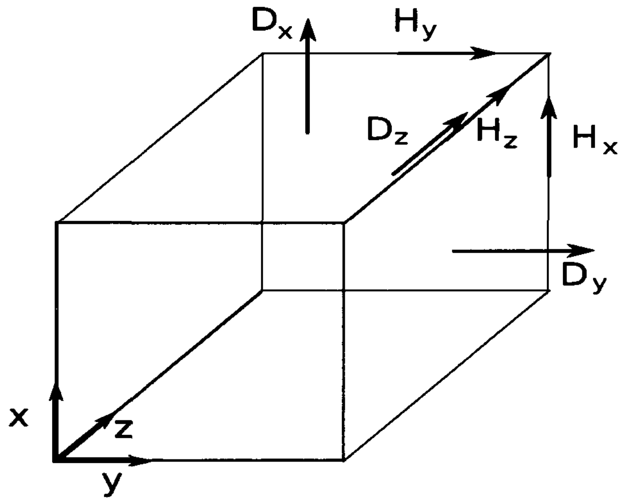

Figure 3.1: *Yee Cell*

We use the notation $D_x^n(i, j, k)$ for the x component of the $\vec{D}$ field at time step n and position $(i\Delta x, j\Delta y, k\Delta z)$. Substituting the central difference approximation for the time and space derivatives, for example ,

$$\frac{\partial D_x}{\partial t} = \left(D_x^{n+1} - D_x^n\right)/\Delta t \tag{3.4}$$

and

$$\frac{\partial H_x}{\partial y} = \left(H_x(i+\frac{1}{2}, j+1, k+1) - H_x(i+\frac{1}{2}, j, k+1)\right)/\Delta y, \tag{3.5}$$

we can obtain discrete versions of Eq. 3.1 and Eq. 3.3. One such example is

$$\begin{aligned} D_z^{n+1}(i+\frac{1}{2},j+\frac{1}{2},k+1) &= D_z^n(i+\frac{1}{2},j+\frac{1}{2},k+1) \\ &+ \frac{c\Delta t}{\Delta x}\left(H_y^{n+\frac{1}{2}}(i+1,j+\frac{1}{2},k+1) - H_y^{n+\frac{1}{2}}(i,j+\frac{1}{2},k+1)\right) \\ &- \frac{c\Delta t}{\Delta y}\left(H_x^{n+\frac{1}{2}}(i+\frac{1}{2},j+1,k+1) - H_x^{n+\frac{1}{2}}(i+\frac{1}{2},j,k+1)\right) \end{aligned} \tag{3.6}$$

Similar equations are derived for the components of $\vec{H}$ and the remainder of the components of $\vec{D}$.

In order to ensure that this algorithm is stable, field propagation through a cell cannot exceed the speed of light. This restriction will determine the relationship between the time step and the grid size. For a one dimensional simulation, this relationship is simple to determine. Since we have only one spatial step size, we know that the time it would take to cross the cell at the speed of light is $\Delta t = \frac{\Delta x}{c_0}$. This equation gives the maximum allowed time step for Δx. For a three dimensional simulation, the limit for Δt was derived using complex-frequency analysis [67]. From this, it was found that the limit for the time step is given by

$$\Delta t_{limit} = \frac{1}{c\sqrt{\frac{1}{(\Delta x)^2} + \frac{1}{(\Delta y)^2} + \frac{1}{(\Delta z)^2}}} \tag{3.7}$$

This gives a relationship between Δx, Δy and Δz and the maximum time step to ensure numerical stability.

The FDTD code used for this thesis is capable of running multiple processes in parallel. The parallalization uses domain decomposition to subdivide the computational work amongst many processors, and uses a Message Passing Interface (MPI) protocol for intercommunication. In domain decomposition, the simulation volume is divided into multiple smaller volumes (Fig. 3.2), and each instance of the code only updates the fields in one of the smaller volumes. As we can see from Eq. 3.6, the FDTD algorithm is such that a field at a particular

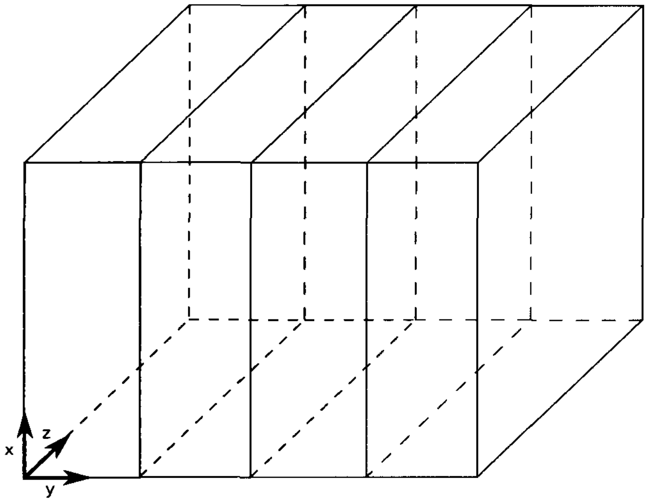

Figure 3.2: *Simulation space decomposed into four domains. Each domain is identified by a different colour.*

location is updated using only the fields from adjacent grid cells. Thus to complete all the field updates at each time step, only the fields at the boundaries of the smaller volumes need to be communicated between parallel processes. For example, in Fig. 3.3, we see that in order to calculate the H_x^p field, we only need the D_z^{p+1} field from the neighbouring processor. This technique of parallelization is very efficient because the intercommunication time scales as the surface area (L^2, where L is the number of grid points along one side of the volume), whereas the computation time scales as the volume size (L^3). The current version of the code has been parallelized in the x-direction and y-direction giving us two dimensions of parallelization. While this portion of the code was inherited, it was necessary to incorporate the parallelization scheme into all the various subroutines and functions that were added to the code for this thesis.

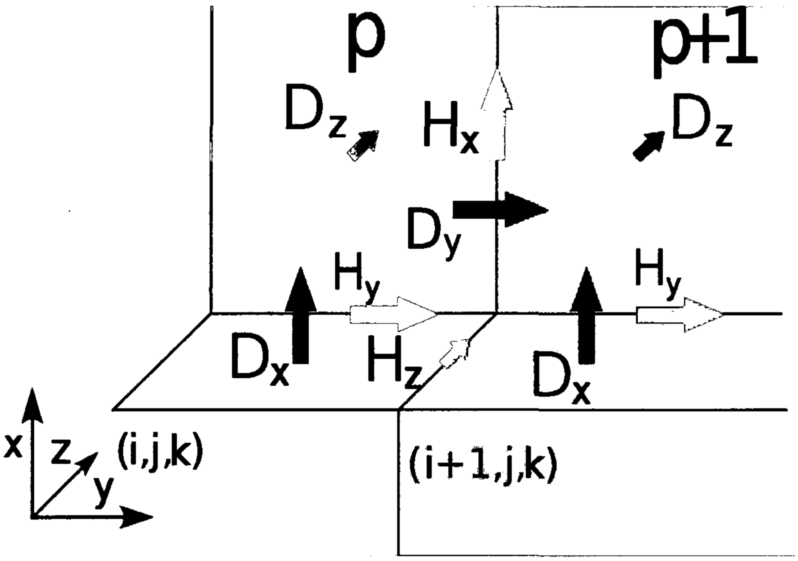

Figure 3.3: *Two cells at the boundary of adjacent processors including the field components as in the Yee cell.*

3.2 Sources

While the section above described how to simulate the propagation of light, in order for there to be nonzero fields within the simulation, we need to introduce sources for the fields. In general, the numerical implementation of the source is required to be as accurate as possible while being specified in a minimum number of cells. This ensures accurate results with the bulk of the computational time and memory dedicated to calculating the unknown outcome of the incident source on the material in the simulation volume.

We have used two similar methods to achieve this. The first is the hard source. For this method, the electric field at a specified position or positions is set equal to a given value determined by an analytical formula that describes the desired source. Specifying the source in a plane allows for numerous types of sources to be incorporated, such as plane waves and Gaussian beams. However, this method causes the location of the source to act as metallic interface. This is easy to see in the case of a source that becomes zero after a certain amount of time. Then the tangential electric field at the location of the source is set to zero exactly as it would be in a metal, resulting in a complete reflection of any propagating field that is incident on the source. This is also true when the value of the electric field is set to any arbitrary value.

The second method used to create external sources is the soft source. Like the hard source, the electric field of the source is specified at a certain position or positions. Unlike the hard source, it does not result in reflections. Instead of setting the value of the electric field at the source location to be exactly the source value, the source electric field values are added to the previous value of the electric field obtained by the regular FDTD update. This allows incident waves to pass through the source undisturbed.

For a general sinusoidal source with a polarization vector $\vec{\pi}$, the soft source update equation is

$$\vec{E}^n(i,j,k) = \vec{E}^{n-1}(i,j,k) + Re(\vec{S}^n(i,j,k)e^{I\omega n\Delta t}) \cdot \vec{\pi} \tag{3.8}$$

To create a hard source, the $\vec{E}^n(i,j,k)$ would be omitted on the right side of the equation. In Sections 3.2.1 and 3.2.2, the form of S is discussed for a plane wave source and a Gaussian beam source, respectively. The polarization vector is discussed in Section 3.2.3.

3.2.1 Plane Waves

One of the two spatial functional forms we used in our simulations is the plane wave. The source is uniform in the directions perpendicular to the direction of propagation. For a plane wave, the source is set at a subset of the grid, corresponding to each grid point on a plane perpendicular to the direction of propagation, at a specific location in the direction of propagation, as illustrated in Fig. 3.4. Each point on the plane has the same numerical value:

$$S^n(i,j,k) = A \tag{3.9}$$

where A is the amplitude of the source.

Though uniform in space, the plane wave source may have an arbitrary profile in time. To simulate a Gaussian pulse envelope in time, we need to specify the width of the pulse σ, and

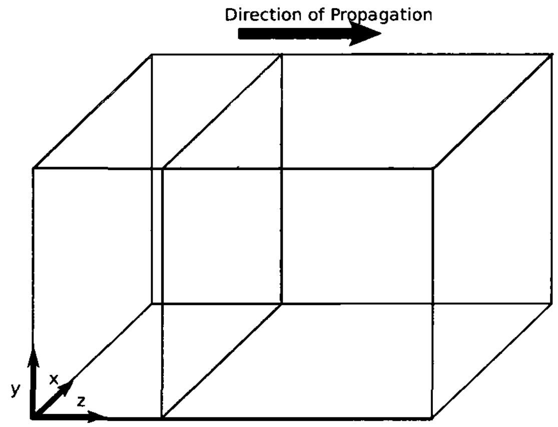

Figure 3.4: *Simulation space. The highlighted plane is initialized at a constant value at each time step for a plane wave.*

the position in time of the centre of the pulse t_0. We find

$$S^n(i,j,k) = Ae^{-(\frac{n\Delta t - t_0}{\sigma})^2} \tag{3.10}$$

where A is the amplitude of the source (Fig. 3.5).

3.2.2 Gaussian Beam

We would also like to be able to describe sources that are not uniform in space. For example, we would like to be able to emulate a laser source to be able to compare our results with experiments. The best approximation for the spatial profile of a paraxial laser beam is a Gaussian beam. The spatial intensity profile of a Gaussian beam is

$$I(x,y,z) \propto |E_0|^2 e^{-\frac{2(x^2+y^2)}{w^2}} \tag{3.11}$$

To implement this as a source in our code, we need an analytical expression for the electric field. We take the source location to be along a plane perpendicular to the propagation direc-

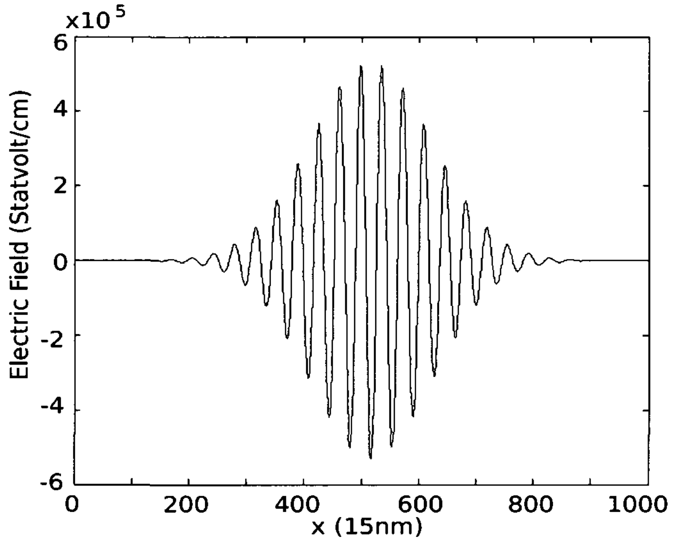

Figure 3.5: *Plane wave with Gaussian envelope in time*

tion, as in Fig. 3.4, but this time we consider that the source will have varying amplitude in space. We set the propagation direction to be in the z-direction. In this thesis, we include the longitudinal component of the Gaussian beam, and although we remain in the paraxial regime, we identified how to go beyond the usual paraxial approximation if necessary. We follow the approach of Chen et al [12]. When $\lambda/(2\pi w_0) < 1$, they obtain the expansion for the source electric field

$$S^n(i,j,k) = S^{(0),n}(i,j,k) + \left(\frac{\lambda}{2\pi w_0}\right)^2 S^{(2),n}(i,j,k) + \dots \tag{3.12}$$

$$S^n_{\|}(i,j,k) = \left(\frac{\lambda}{2\pi w_0}\right) S^{(1),n}_{\|}(i,j,k) + \left(\frac{\lambda}{2\pi w_0}\right)^3 S^{(3),n}_{\|}(i,j,k) + \dots, \tag{3.13}$$

where w_0 is the 1/e distance of the beam at the focus and λ is the wavelength of light. $S^n(i,j,k)$ is the component of the source electric field in the plane perpendicular to the direction of propagation, in our case, the x-y plane, and $S^n_{\|}(i,j,k)$ is the component of the source electric field in the direction of propagation, the z-direction. This expansion reduces to the paraxial approximation if $\lambda/(2\pi w_0) \ll 1$ and only the $S^{(0),n}(i,j,k)$ is appreciable in that case. For this source, the polarization determines the orientation of $S^n(i,j,k)$ in the x-y plane and corresponds to the source term in Eq. 3.8. Similarly, the component of the field in the direction of propagation is updated by

$$E_z^n(i,j,k) = E_z^n(i,j,k) + S_{\|}^n(i,j,k) \tag{3.14}$$

where $E_z^n(i,j,k)$ is the field calculated by the FDTD update equations in the direction of propagation.

For this thesis, we are near the paraxial regime and therefore, we can approximate the electric field by the first two terms, $S^{(0),n}(i,j,k)$ and $\lambda/(2\pi w_0)S_{\|}^{(1),n}(i,j,k)$. The component in the plane perpendicular to the propagation is given by [6]

$$S^n(i,j,k) = S^{(0),n}(i,j,k) = \frac{A}{1+I\xi}e^{-\frac{r^2}{w_0^2(1+I\xi)}} \tag{3.15}$$

$$\xi = \frac{2k\Delta z}{b}, b = \frac{2\pi w_0^2}{\lambda} \tag{3.16}$$

In this section, we use $I = \sqrt{-1}$ to avoid confusion with the index in the x-direction, i. The position of the beam's focus is at $z = 0$. For substitution into Eq. 3.8, Eq. 3.15 becomes

$$Re(Se^{I\omega\Delta t}) = \frac{A}{1+\xi^2}e^{-\frac{r^2}{w_0^2(1+\xi^2)}}(\cos\alpha + \xi\sin\alpha) \tag{3.17}$$

$$\alpha = \frac{\xi r^2}{w_0^2(1+\xi^2)} - \omega n\Delta t \tag{3.18}$$

The component in the direction of propagation is given by [12]

$$S_{\|}^n = S_{\|}^{(1),n}(i,j,k) = -\frac{Ii\Delta x}{w_0}\frac{1}{(1+I\xi/2)^2}e^{-\frac{r^2}{2w_0^2(1+I\xi/2)}}e^{I\omega n\Delta t} \tag{3.19}$$

Simplifying this expression and taking the real part, we find the update equation for the z-

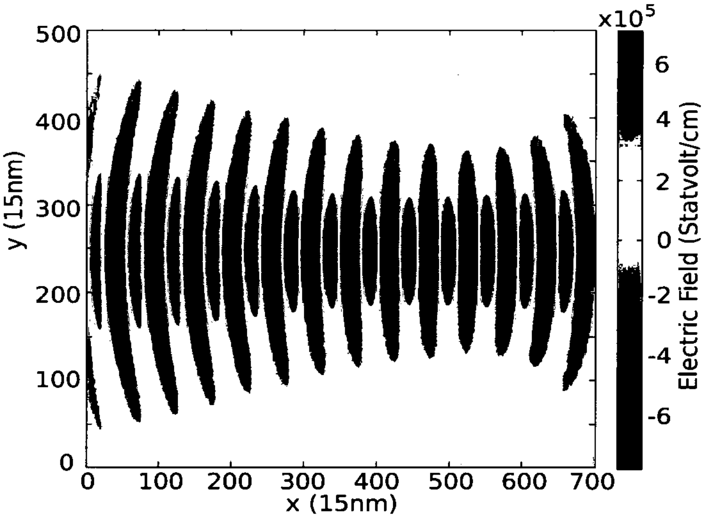

Figure 3.6: *Gaussian beam focused at* $x = 500$

component of the electric field:

$$\begin{aligned}
E_z^n(i,j,k) &= E_z^n(i,j,k) + \left(\frac{\lambda}{2\pi w_0}\right)\gamma e^{\frac{-r^2}{2w_0^2+w_0^2\xi^2/2}} \\
\gamma &= \frac{i\Delta x(1-\xi^2/4)}{x_0[(1-\xi^2/4)^2+\xi^2]}\sin\beta - \frac{i\Delta x\xi}{x_0[(1-\xi^2/4)^2+\xi^2]}cos\beta \\
\beta &= \frac{r^2\xi}{4w_0(1+\xi^2/4)} + \omega n\Delta t
\end{aligned} \tag{3.20}$$

When this source is implemented in the first cell in the propagation direction, the electric field displays a Gaussian profile in the directions perpendicular to the propagation direction. It also has a decreasing 1/e distance as it approaches the focus and an increasing 1/e distance beyond the focus (Fig. 3.6).

A physical laser is a pulsed Gaussian in time. Therefore, we must multiply our beam profile by a Gaussian in time as we have done with the plane wave source. For example, the source term in the direction parallel to the propagation is

$$S^n(i,j,k) = \frac{A}{1+I\xi}e^{-\frac{r^2}{w_0^2(1+I\xi)}}e^{-(\frac{n\Delta t-t_0}{\sigma})^2} \tag{3.21}$$

Using this form, we get the correct form for a pulsed Gaussian beam (Fig. 3.7).

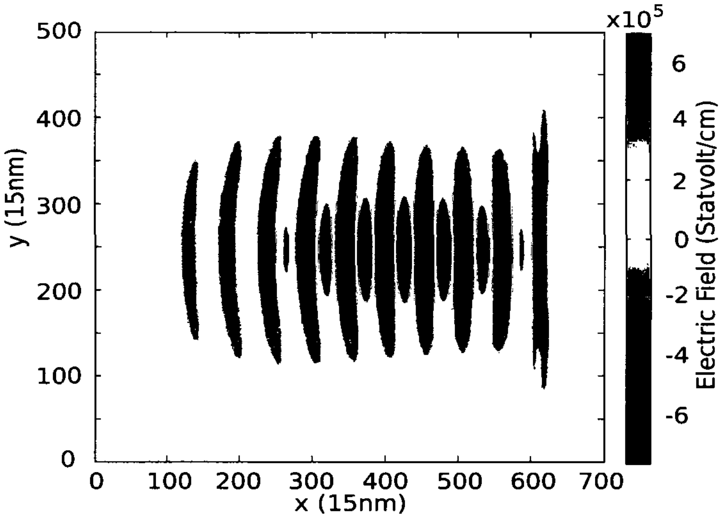

Figure 3.7: *Pulsed Gaussian beam*

This source must be compatible with a simulation volume subdivided into domains for parallel processing. The analytical equations for the beam source require the positions, (i, j, k), to be relative to the entire simulation space, however, the cell positions updated in the FDTD equations are relative to the processor. When only one processor is used in the source plane, these two positions are identical. If the parallelization is in the plane perpendicular to the direction of propagation, the source will range over different processors (Fig. 3.8). Therefore, information concerning the processor number and its neighbours must be utilized to transform the cell number to its position relative to the entire simulation space. When the simulation space is parallelized in the direction of propagation, the processor number must be considered to ensure that the source is only implemented once and at the correct position.

3.2.3 Polarization

In addition to the spatial and temporal profiles of the source, the source polarization must also be set. We have implemented sources for both linearly polarized and circularly polarized light.

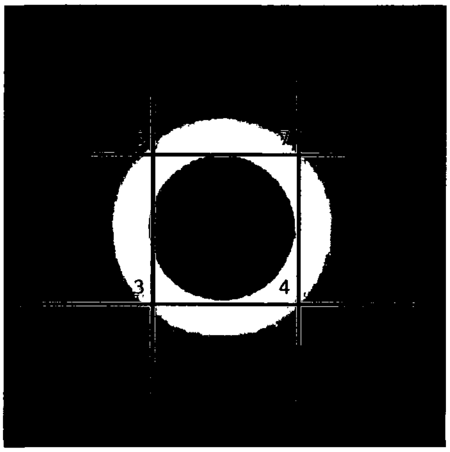

Figure 3.8: *Gaussian source split among 9 processors. Processor number indicated in bottom right corner of cell.*

For linearly polarized light, the orientation of the electric and magnetic fields at the source location is constant. We take the direction of propagation to be the z-direction. In symmetric materials, this can be modeled by adding the source to the x-component of the field, since any direction can be chosen as the x-direction. For a medium that is not symmetric, where the angle of polarization to the x-axis is important, the polarization vector is

$$\vec{\pi} = \cos\theta\hat{x} + \sin\theta\hat{y} \tag{3.22}$$

where θ is the angle of polarization with respect to the x-axis.

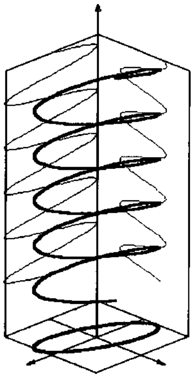

Figure 3.9: *For elliptically polarized light, $\vec{E}$ and $\vec{H}$ fields transcribe an ellipse over time.*

Circularly polarized light is a special case of elliptically polarized light. Elliptically polarized light has a dynamic orientation of electric and magnetic fields. The direction of the $\vec{E}$ and $\vec{H}$ fields transcribes an ellipse in a fixed plane perpendicular to the direction of propagation (Fig. 3.9). The polarization vector is then given by

$$\vec{\pi} = E_{10}\cos(\omega n\Delta t)\hat{x} + E_{20}\sin(\omega n\Delta t)\hat{y} \tag{3.23}$$

where E_{10} is the amplitude in the x-direction and E_{20} is the amplitude in the y-direction. If $E_{10} = E_{20}$, then the field is left circularly polarized. If $E_{10} = -E_{20}$, then the field is right circularly polarized. In our code, we only simulate right and left handed circular polarization.

The polarization is set in addition to the time dependence of the pulse envelope function, and the spatial profile, as seen in Eq. 3.8.

3.3 Boundary Conditions

One of the drawbacks of the FDTD method is that the simulation space must be finite in size. Since in most physical systems, the fields propagate past the boundaries of the simulation space, we must determine boundary conditions to simulate an infinite medium. There are numerous methods to determine these boundary conditions and each differs depending on the effect required. For our purposes, we have implemented three options for boundary conditions: Periodic, Total Field/Scatter Field (TF/SF) and Perfectly Matched Layer (PML).

3.3.1 Periodic Boundary Conditions

The periodic boundary condition is one of the simplest to implement. It is useful for infinite volumes that contain structures that are repeated periodically. One example of such a structure is an infinite array of metallic waveguides (Fig. 2.1). Instead of creating a medium that contains a large number of identical waveguides, we can create a medium containing one waveguide and run the simulation with periodic boundary conditions in the direction of periodicity (the x-direction, in this example). They are also useful for the direction perpendicular to both the propagation direction and the direction of periodicity. In our example, the waveguides have a finite width in the x-direction but are infinite in the y-direction. We can create the waveguides such that they are the length of the simulation space in the y-direction. Thus, by running the simulation with periodic boundary conditions we achieve the effect of our material being repeated infinitely many times in the y-direction giving us an infinitely long wavguide.

To understand how to implement periodic boundary conditions, it is necessary to know the details of the simulation volume boundaries and the FDTD algorithm. In general, when updating the fields in a grid cell, the values of the fields in neighbouring grid cells are required. Considering the z-direction, the boundary cells of the simulation volume are at 1 and N_z, which means the fields at cells 0 and $N_z + 1$, respectively, are required for the updates. A ghost cell layer that runs along the whole outer boundary of the simulation space is created to hold these values. To implement periodic boundary conditions, the field values corresponding to the ghost cells are set as follows: The fields at $k = N_z$ are put into the ghost cells at $k = 0$, and the fields at $k = 1$ are put into the ghost cells at $k = N_z + 1$. This is repeated in the x- and y- directions, as required. The ghost cells are set after each field ($\vec{H}$ and $\vec{E}$) is updated by the main FDTD algorithm, in preparation for the next loop.

3.3.2 Total Field/Scatter Field

The Total Field/Scatter Field (TF/SF) formulation separates the simulation space into two regions — the total field region and the scatter field region. The total field region is the larger central portion of the simulation space and it contains any interesting properties of the medium to be studied. In this region, the fields are the physical fields including the incident light and all scattered light. The scatter field region is the area around the total field region near the boundaries. In this region, only the fields scattered from the medium are present, the source field is removed. The two regions are separated in this manner so that the energy from the source (which is not present in the scatter region) does not reach an absorbing boundary and the field reflected from the edges of the simulation volume is further minimized [65].

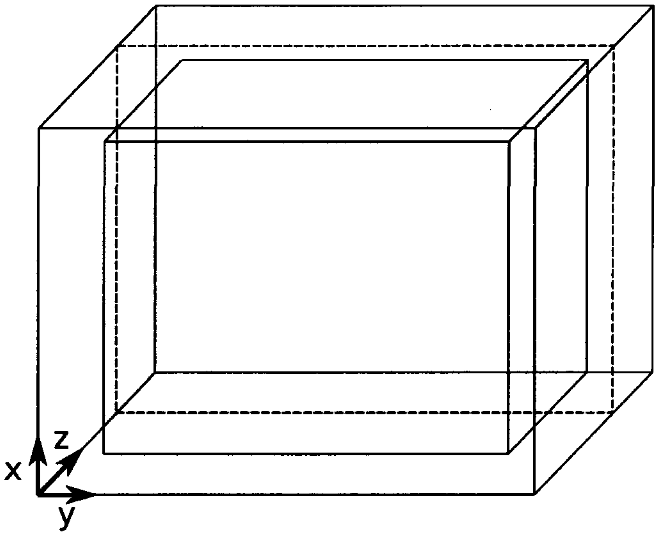

Figure 3.10: *The larger rectangle is the entire simulation space while the inner rectangle is the total field region. The region outside the total field region is the scatter field region. The dotted rectangle indicates the 2D cut through the simulation space that will be used for this discussion.*

Since the source field must be added or subtracted from the boundaries between the two regions, the TF/SF is easiest to implement for plane wave sources where the field is uniform in two dimensions.

If TF/SF is implemented along all of the boundaries, the two regions are separated as seen in Fig. 3.10. For simplicity, we will examine a two-dimensional cut through a simulation volume (Fig. 3.11(a)). We assume the light propagates in the x-y plane, therefore, for a plane wave source, the only non-zero components of the field are E_z, H_x and H_y.

Each component of the fields is either in the total field region or in the scattered field region. However, when the fields are updated along the boundary, the standard update equations include fields from both the total field and scatter field regions. We must introduce a new subroutine to correct these fields so that the updates include only total field terms or only scatter field terms. This can be done by adding or subtracting the known source term at the TF/SF boundaries. We relate the total and scattered fields via

$$\vec{E}_{tot} = \vec{E}_{scatt} + \vec{E}_{inc} \tag{3.24}$$

where $\vec{E}_{tot}$ is the total field, $\vec{E}_{scatt}$ is the scattered field and $\vec{E}_{inc}$ is the incident field. As is seen in Fig. 3.11, at the boundaries $j = j_a$, $j = j_b$, $i = i_a$ and $i = i_b$ the FDTD update equations include both total fields and scatter fields. For example, in Fig. 3.11(b), at the $j = j_a$ boundary, the FDTD update equation for $H_x(i, j_a - \frac{1}{2})$ is

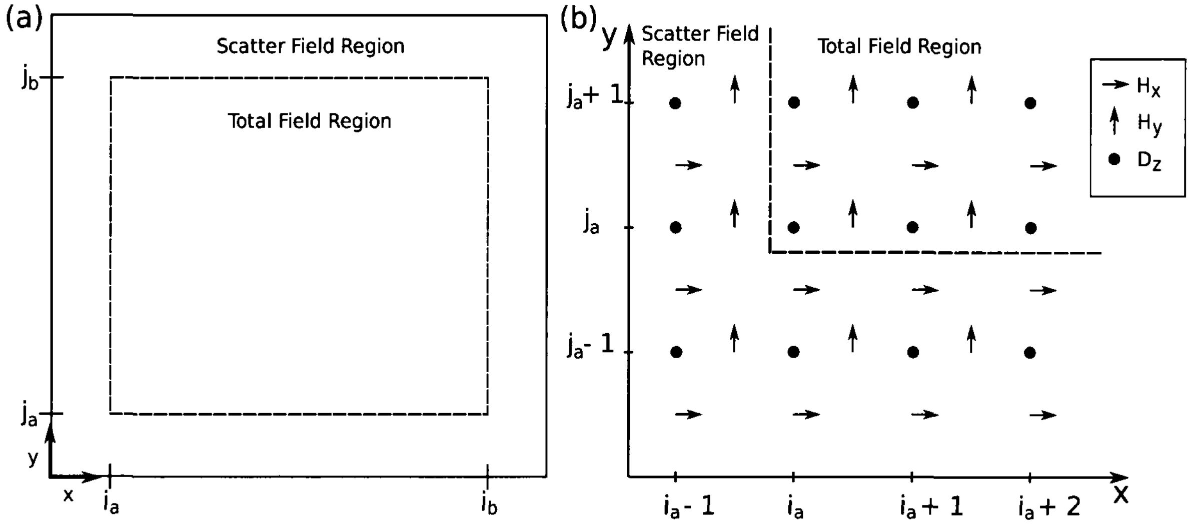

Figure 3.11: *(a) The 2D cut through the 3D simulation space in Fig. 3.10 (b) The lower left corner of (a). The dotted line represents the border between the total field and scatter field regions. The dots represent the D_z field while the arrows represent the H_x and H_y fields.*

$$H^{n+\frac{1}{2}}_{x,scatt}(i, j + \frac{1}{2}) = H^{n-\frac{1}{2}}_{x,scatt}(i, j + \frac{1}{2}) - \frac{c\Delta t}{\Delta y}(E^n_{z,tot}(i, j + 1) - E^n_{z,scatt}(i, j)) \tag{3.25}$$

In order to eliminate the $E_{z,tot}$, we must subtract $E_{z,inc}$.

$$\begin{aligned} H^{n+\frac{1}{2}}_{x,scatt}(i, j + \frac{1}{2}) &= H^{n-\frac{1}{2}}_{x,scatt}(i, j + \frac{1}{2}) \\ &- \frac{c\Delta t}{\Delta y}\left((E^n_{z,tot}(i, j + 1) - E_{z,inc}(i, j + 1)) - E^n_{z,scatt}(i, j)\right) \end{aligned} \tag{3.26}$$

Thus, if we correct for the TF/SF after the FDTD update, our correction equation will be

$$H^{n+\frac{1}{2}}_{x,scatt}(i, j + \frac{1}{2}) = H^{n-\frac{1}{2}}_{x,scatt}(i, j + \frac{1}{2}) + E_{z,inc}(i, j + 1) \tag{3.27}$$

Similar equations can be derived for the remaining boundaries.

In order to determine the incident fields, we introduce an one-dimensional auxiliary array. In this array, a sinusoidal hard source is implemented in the first cell and propagated along the array using one-dimensional FDTD update equations. Since a plane wave is uniform in the direction perpendicular to its propagation, this one-dimensional source can be extrapolated to a two- or three-dimensional plane wave source.

For plane wave propagation in the direction of one of the axes, the extrapolation from the one-dimensional source to the TF/SF boundaries is straight forward. The incident field is equal to the source at the position in the propagation direction. In our two-dimensional example, if the direction of propagation is the y-direction, then $E_{z,inc}(i, j) = E_{inc}(j)$ where E_{inc} is the one-dimensional source.

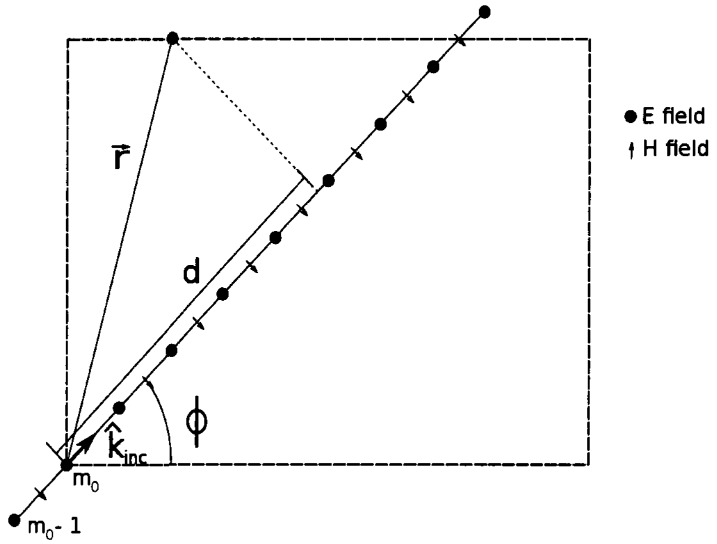

Figure 3.12: *The simulation space with a source incident at an angle ϕ. The dotted box indicates the total field region. The straight line indicates the auxilary source array. The source must be extrapolated to the edge of the total field region at arbitrary $\vec{r}$ values.*

For plane wave propagation at an angle to one of the axes, the extrapolation of the one-dimensional source array to the TF/SF boundaries is not as simple. Let us take our two-dimensional example and assume a plane wave is propagating at an angle of ϕ to the y-axis (Fig. 3.12). In the one-dimensional source array, let us assume there is a point m_0 where the auxilary incident electric field corresponds to the electric field at the corner of the total field region such that

$$E_{inc}(m_0) = E_{z,inc}(i_a + \frac{1}{2}, j_a + \frac{1}{2}). \tag{3.28}$$

For some arbitrary cell (i, j) in the total field region, we find

$$\begin{aligned} \vec{r} &= \left((i + \frac{1}{2})\Delta x - (i_a + \frac{1}{2})\Delta x\right)\hat{x} + \left((j + \frac{1}{2})\Delta y - (j_a + \frac{1}{2})\Delta y\right)\hat{y} \\ &= (i - i_a)\Delta x\hat{x} + (j - j_a)\Delta y\hat{y} \end{aligned} \tag{3.29}$$

We define $\hat{k}_{inc}$ as the unit vector in the direction of propagation. The field at the point $\vec{r}$ will be the same as the field at its projection on a line in the direction of $\hat{k}_{inc}$. This will be a value in the one-dimensional source array. The length of this projection is the dot product of $\hat{k}_{inc}$ and $\vec{r}$,

$$d = \hat{k}_{inc} \cdot \vec{r} \tag{3.30}$$

$$= (i - i_a)\Delta x \sin\phi + (j - j_a)\Delta y \cos\phi. \tag{3.31}$$

We need to determine the index of the source array from d. The number of cells that d spans in the source array is $n = d/\Delta + m_0$ where Δ is the step size of the source array. Since in general n is not an integer, the field at our arbitrary point is a linear combination of two cells in the source array. Let the remainder of d/Δ be δ. Thus the value of the field at our arbitrary point is

$$E_{z,inc}(i + \frac{1}{2}, j + \frac{1}{2}) = (1 - \delta)E_{inc}\left(mod\left(\frac{d}{\Delta}\right) + m_0\right) + \delta E_{inc}\left(mod\left(\frac{d}{\Delta}\right) + m_0 + 1\right) \tag{3.32}$$

Similar equations can be derived for the remaining fields. An example of a plane wave propagating at an angle with TF/SF boundary conditions is shown in Fig. 3.13

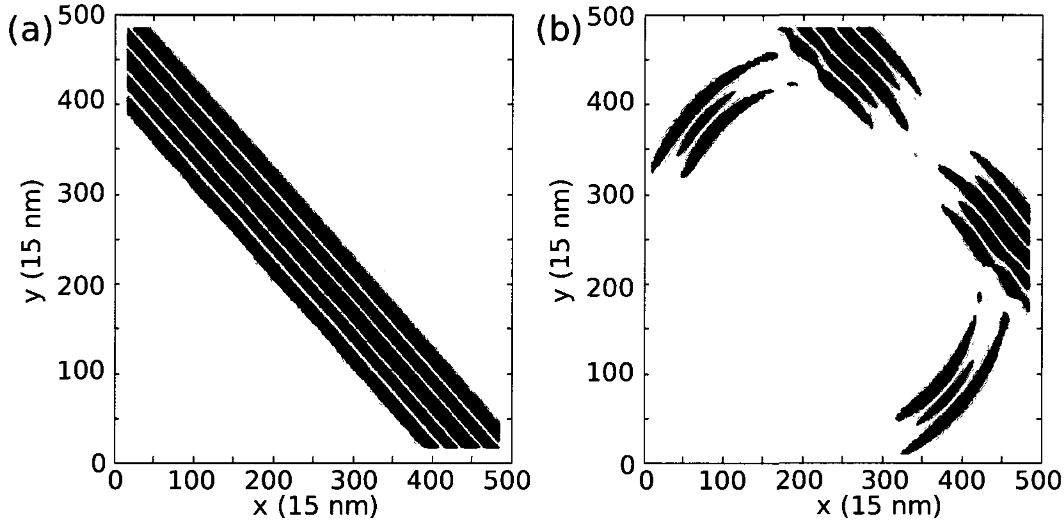

Figure 3.13: *Plane wave with Gaussian envelope in time propagating at an angle of* $\frac{\pi}{4}$ *with Total-Field Scatter-Field boundary conditions (a) with and (b) without a metallic cube.*

This method can easily be extended to three-dimensions, and that is what we have implemented in the code. The update equations presented in this section are valid for the three-dimensional case. In addition to these updates, two additional boundaries must be updated. This method was further extended so that the TF/SF boundary conditions could be applied in parallel processing.

Since the incident field must be known at all boundary points, it is inefficient to use this method for many types of sources. Too much computation time and memory would be used if we calculated the incident field at every point in the simulation space. Therefore, this method is intended for sources that can easily be extrapolated from a one-dimensional source such as a plane wave.

3.3.3 Perfectly Matched Layer (PML)

The perfectly matched layer (PML) is an absorbing boundary used when the simulation requires that all the fields continue to propagate out of the simulation space, without reflection. This is achieved by implementing a PML that serves to absorb all of the energy that comes in contact with the boundaries without reflecting any of the incident light. The PML is unique in that it is effective over a broad bandwidth and arbitrary incident angle. The PML is essentially an artificial material, whose properties we describe below.

In general, when a wave is incident on a boundary between two materials, the reflection coefficient is given by

$$R = \frac{\eta_A - \eta_B}{\eta_A + \eta_B} \tag{3.33}$$

where $\eta = \sqrt{\frac{\mu}{\epsilon}}$. If $R = 0$ then there will be no reflection. This is ideal for an absorbing boundary condition because there are no spurious reflections from the artificial boundary to interfere with the desired signal. Thus we need $\eta_A = \eta_B$. However, we also want this material to be lossy such that the transmitted field is entirely absorbed. This we can achieve by allowing μ and ϵ to be complex.

To implement this, we introduce fictional dielectric constants and permeabilities [65]. Transforming Maxwell's equations into the frequency domain and introducing the fictional dielectric constants ($\bar{\epsilon}$) and permeabilities ($\bar{\mu}$), we get

$$I\omega\vec{D}\bar{\epsilon} = c\vec{\nabla} \times \vec{H} \tag{3.34}$$

$$\vec{D} = \epsilon_r\vec{E} \tag{3.35}$$

$$I\omega\vec{H}\bar{\mu} = -c\vec{\nabla} \times \vec{E} \tag{3.36}$$

We have two conditions on $\bar{\epsilon}$ and $\bar{\mu}$. First, as discussed above, the impedance must be constant across the boundary. Second, the relative dielectric constant and the relative permeability must be the inverse of each other in the direction perpendicular to the boundary to allow for complete absorption. Following these conditions, we find that the form of the fictional dielectric constants and permeabilities is

$$\bar{\epsilon} = \begin{pmatrix} \gamma_x^{-1}\gamma_y\gamma_z & 0 & 0 \\ 0 & \gamma_x\gamma_y^{-1}\gamma_z & 0 \\ 0 & 0 & \gamma_x\gamma_y\gamma_z^{-1} \end{pmatrix}$$

$$\gamma_m = 1 + \frac{\sigma_m}{I\omega\epsilon_0} \tag{3.37}$$

where $m = x, y, z$. If we then increase σ as we approach the end of the simulation space, this will absorb a large portion of the incident field thereby creating a non-reflecting, absorbing boundary.

3.3.4 Applicability of Boundary Conditions

We now have described three sets of boundary conditions: Periodic, TF/SF and PML. However, they cannot be applied arbitrarily to every situation as each condition has different advantages and disadvantages. In this section, we summarize their applicability.

Periodic boundary conditions are used to simulate an infinitely periodic medium such as free space or a periodic array of parallel waveguides. Both a plane wave and a Gaussian source can be simulated with these boundary conditions. However, when implementing a Gaussin beam with periodic boundary conditions, the simulation space must be large enough to ensure that the source is zero at the boundaries. In general, periodic boundary conditions would not be used along the propagation direction because this would create a source at both ends of the simulation space.

The TF/SF boundary condition can only be implemented efficiently for a plane wave source. However, it is the only method for introducing an angled source. It is most useful when a plane wave source is required but the simulation space is not periodic and is often used in conjunction with PML boundary conditions which absorb the scattered field. To extend this method for use with other sources such as a Gaussian source, an additional 3D simulation must be solved for the source propagation through an empty simulation volume, which is very computationally intensive and cumbersome, and thus not commonly used.

PML boundary conditions are absorbing boundary conditions. They simulate the fields incident on the boundaries propagating to infinity. This is very useful because a small simulation space can model a system in free space. However, if a source is in contact with the PML, the energy will be absorbed and the source will not propagate properly. Therefore, the source must be set outside of the PML and must not propagate along the PML boundaries. In the case of a plane wave the source needs to be protected by a TF/SF boundary if the PML is used along the boundary faces parallel to the propagation direction. In the case of a Gaussian beam, if the simulation space is large enough to ensure that the source is zero at the boundaries, PML boundary conditions are suitable.

3.4 Materials

Up to this point, we have described the propagation of light in a vacuum. We now need to determine the effect of a nonlinear, dispersive medium. As mentioned at the beginning of this chapter, all of the properties of the material are implemented via Eq. 3.2. Since this equation depends on the polarization ($\vec{P}$), it can be used to model both linear and non-linear properties of a material in time or frequency space. For this thesis, we have developed a code that simulates simple dielectrics, plasmas (through the Drude model), multiphoton ionization, avalanche ionization, and the Kerr effect. For the latter four, we developed our own algorithms based on theoretical equations describing these processes.

We write Eq. 3.2 as a sum of several polarization vectors, one for each process that we are interested in modeling:

$$\vec{D}(\vec{r},t) = \epsilon_r \vec{E}(\vec{r},t) + 4\pi \left(\vec{P}_D(\vec{r},t) + \vec{P}_{MP}(\vec{r},t) + \vec{P}_{Kerr}(\vec{r},t) \right) \tag{3.38}$$

where $\epsilon_r \vec{E}$ represents the linear, frequency-independent dielectric response of the material, $\vec{P}_D$ is the polarization due to the dispersive response of the material, $\vec{P}_{MP}$ causes absorption of the field due to multiphoton (in our case six-photon) ionization and $\vec{P}_{Kerr}$ includes the effects of the third-order Kerr nonlinearity.

To simulate the non-linear ionization of a dielectric, Eq. 3.38 is coupled to an equation that describes the plasma creation which is given by

$$\frac{dN(\vec{r},t)}{dt} = R_{av}(\vec{r},t) + R_{MP}(\vec{r},t) \tag{3.39}$$

where $N(\vec{r},t)$ is the spatially dependent free electron density, $R_{av}(\vec{r},t)$ is the contribution due to avalanche ionization and $R_{MP}(\vec{r},t)$ is the contribution of multiphoton ionization.

In this section, we will describe the theory and implementation of each process in Eq. 3.38 and 3.39.

3.4.1 Linear Regime

In the case of a linear, frequency independent dielectric material, the relation between the $\vec{D}$ and $\vec{E}$ fields is simply

$$\vec{D} = \epsilon_r \vec{E} \tag{3.40}$$

Thus creating different materials merely requires different values for ϵ_r. By using a data file with the values of ϵ_r at each cell to specify the material, we can simulate the propagation through complicated structures easily. For structures that are not square at their edges, an average value is used for any cell that is partially inside the structure (Fig. 3.14).

3.4.2 Frequency Dependent Materials and Drude Model

If a material has a frequency dependent response to light, the $\vec{E}$ field cannot be related to the $\vec{D}$ field by a constant. In general, the relationship between $\vec{E}$ and $\vec{D}$ for a linear dispersive

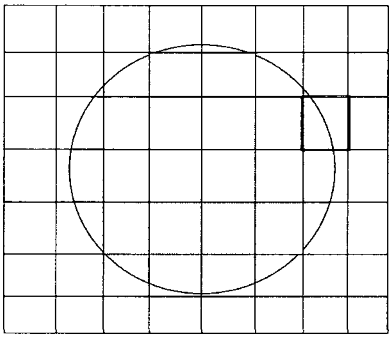

Figure 3.14: *A circle with a different index of refraction on a grid. If no averaging of the index of refraction was done, the yellow squares would make up the circle. A weighted average of the index of refraction is done for cells with part of the circle enclosed such as in the red grid point.*

medium is

$$\tilde{D}(\omega) = \tilde{\epsilon}(\omega)\tilde{E}(\omega) \tag{3.41}$$

where $\tilde{D}(\omega)$ and $\tilde{E}(\omega)$ represent the Fourier transforms of the $\vec{D}$ and $\vec{E}$ fields in the frequency domain. We use the Drude model to describe the frequency dependent response of the free electron plasma. Therefore, we take

$$\tilde{\epsilon}(\omega) = 1 - \frac{\omega_p}{\omega(\omega - I\Gamma)} \tag{3.42}$$

Since the FDTD updates are in the time domain, we need to transform Eq. 3.41 from the frequency domain into the time domain. When this is done with Eq. 3.42 substituted into Eq. 3.41, we obtain a convolution of $\epsilon(t)$ and the electric field [67]. This convolution then needs to be made discrete.

The Drude model is derived from the Lorentz equation of motion for a charged particle in a medium interacting with an electric field $\vec{E}$,

$$m\ddot{x} + m\Gamma\dot{x} = -eE \tag{3.43}$$

where x is the displacement of the particle, m is the mass of the charged particle, e is the charge of the particle, Γ is the relaxation time and $\dot{x} = \frac{dx}{dt}$. Fourier transforming this equation into the frequency domain, we get

$$m(I\omega)^2\tilde{x}(\omega) + I\omega m\Gamma\tilde{x}(\omega) = -e\tilde{E}(\omega) \tag{3.44}$$

Solving this equation for $\tilde{x}(\omega)$ gives

$$\tilde{x}(\omega) = \frac{e}{m}\frac{\tilde{E}(\omega)}{\omega(\omega - I\Gamma)} \tag{3.45}$$

Fourier transforming $\tilde{x}(\omega)$ back into the time domain we get

$$x(t) = \frac{e}{m\Gamma}\int_{-\infty}^{t}[1 - e^{-\frac{\Gamma}{(t-t')}}]E(t')dt' \tag{3.46}$$

The polarization of an ensemble of these particles is given by

$$P_D(t) = eN(t)x(t) \tag{3.47}$$

where $N(t)$ is the density of charged particles. Substituting in our equation for $x(t)$, we find

$$P_D(t) = \frac{\omega_p^2(t)}{4\pi\Gamma}\int_{-\infty}^{t}[1 - e^{-\frac{\Gamma}{(t-t')}}]E(t')dt' \tag{3.48}$$

where $\omega_p^2(t) = (4\pi e^2 N(t))/m_e$ [67] is the plasma frequency.

In order to use these equations in the FDTD method, we need to make them discrete. In Eq. 3.48, the integral becomes a sum over the number of time steps and the electric field becomes the discrete values calculated by the FDTD method at each time step. A similar method for implementing a Debye medium was introduced in Taflove [67]. We modified this method to implement the more complicated convolution of the Drude medium. The sum converted from an integral in Eq. 3.48 is then written as

$$
\begin{aligned}
S^n &= \frac{\Delta t \omega_p^2(t)}{4\pi\Gamma}\left(\sum_{i=0}^{n} E^i - \sum_{i=0}^{n} e^{-\Gamma(n-i)\Delta t} E^i\right) && (3.49) \\
&= (S_1^n - S_2^n) && (3.50)
\end{aligned}
$$

where S^n is the sum at time $n\Delta t$ and we define

$$
\begin{aligned}
S_1^n &= \frac{\Delta t \omega_p^2(t)}{4\pi\Gamma} \sum_{i=0}^{n} E^i \\
S_2^n &= \frac{\Delta t \omega_p^2(t)}{4\pi\Gamma} \sum_{i=0}^{n} e^{-\Gamma(n-i)\Delta t} E^i
\end{aligned}
$$

To implement these equations, S_1^n and S_2^n must be related to S_1^{n-1} and S_2^{n-1}, respectively. For S_1^n, this is straight-forward:

$$
S_1^n = \frac{\Delta t (\omega_p^n)^2}{4\pi\Gamma} E^n + S_1^{n-1} \tag{3.51}
$$

Separating the summation in S_2^n into a sum of the n^{th} value and the summation of $i = 0$ to $n - 1$ we obtain

$$
S_2^n = \frac{\Delta t (\omega_p^n)^2}{4\pi\Gamma} (e^{-\Gamma\Delta t} E^n + \sum_{i=0}^{n-1} e^{-\Gamma(n-i)\Delta t} E^i) \tag{3.52}
$$

We can write S_n^{n-1} as follows

$$
S_2^{n-1} = \frac{(\omega_p^n)^2 \Delta t}{4\pi\Gamma} e^{\Gamma\Delta t} \sum_{i=0}^{n-1} e^{-(n-i)\Gamma\Delta t} E^i \tag{3.53}
$$

Thus, Eq. 3.52 becomes

$$S_2^n = \frac{\Delta t(\omega_p^n)^2}{4\pi\Gamma}(e^{-\Gamma\Delta t}E^n + e^{\Gamma\Delta t}S_2^{n-1}) \tag{3.54}$$

Now we are able to update S_1 and S_2 based on their previous values and the current electric field. Substituting these values into Eq. 3.2, we obtain, finally

$$P_D^n = \left(\frac{(\omega_p^n)^2\Delta t}{\Gamma}E^n + S_1^{n-1}\right) - \left(\frac{(\omega_p^n)^2\Delta t}{\Gamma}e^{-\Gamma\Delta t}E^n + e^{-\Gamma\Delta t}S_2^{n-1}\right) \tag{3.55}$$

3.4.3 Multiphoton Absorption

When a free-carrier is excited to the continuum through this process, multiple photons are absorbed. This causes a decrease in intensity and thus in the electric field of the laser. The decrease in intensity can be modeled as

$$\frac{dI}{dz} = -\sigma I_p I_e^6 \tag{3.56}$$

where I_e is the intensity of the electric field, σ is the 6-photon cross-section and I_p is the band gap. We assume the form for the polarization due to MPI is $\vec{P}_{MPI} = \chi_{MPI}\vec{E}$. From this assumption we find χ_{MPI} to be [10]

$$\chi_{MPI} = \frac{I n_0 c I_p \sigma}{\omega} I_e^5 \tag{3.57}$$

To implent this in the FDTD algorithm, we need to transform it to the time domain. Replacing $I\omega$ with $-\frac{\partial}{\partial t}$ we find

$$\frac{\partial \chi_{MPI}}{\partial t} = n_0 c I_p \sigma I_e^5 \tag{3.58}$$

Performing a finite difference of this equation we derive an update equation for χ_{MPI} given by

$$\chi^{n}_{MPI} = n_0 c I_p \sigma_6 \Delta t (I_e^{n-\frac{1}{2}})^5 + \chi^{n-1}_{MPI} \tag{3.59}$$

This gives a polarization due to multiphoton absorption of

$$P^{n}_{MP} = \chi^{n}_{MPI} E^{n} \tag{3.60}$$

3.4.4 Kerr Nonlinearity

The Kerr nonlinearity, also known as the optical Kerr effect, is a change in the effective refractive index of a material due to nonlinear components of the polarization, in particular, the term arising from the third-order susceptibility. The Kerr effect gives rise to nonlinear effects such as self-focusing and optical solitons. For this thesis, we assume the Kerr effect is instantaneous. Then the change in the index of refraction due to the Kerr effect can be modeled by

$$\Delta n = n_2 I_e \tag{3.61}$$

The corresponding polarization is

$$\vec{P} = \frac{n_0 n_2 I_e}{2\pi} \vec{E} \tag{3.62}$$

This gives an effective χ_{Kerr} of

$$\chi_{Kerr} = \frac{n_0 n_2}{2\pi} I_e \tag{3.63}$$

Our discrete polarization due to the Kerr effect is therefore

$$\vec{P}^{n}_{Kerr} = \chi^{n}_{Kerr} \vec{E}^{n} \tag{3.64}$$

3.4.5 Nonlinear Ionization

Multiphoton Ionization (MPI)

When intense light is incident on a material such that the photon energy is much less than the band gap, and the intensity of the incident beam is large enough, multiphoton ionization becomes important. We will be investigating interaction of fused silica, which has an ionization potential of $9eV$, with $800nm$ light ($1.5eV$ photons). Therefore, we include six-photon absorption in our model.

The MPI process creates charged particles and therefore increases the charge particle density, N. We are interested in understanding how the plasma is created as a function of space and time, and the properties of our dispersive medium are related to N by $\omega_p^2 = \frac{4\pi e^2 N}{m_e}$. Thus we must model the change in N. For six-photon absorption, the contribution from MPI to the rate equation for N is given by [43],

$$R_{MP} = \sigma I_e^6 \tag{3.65}$$

where I_e is the intensity of the electric field. Since I is a function of space and time, N will also be a function of space and time.

Avalanche Ionization

Once a medium has electrons in the conduction band, these electrons can absorb energy from the laser field, and gain enough energy to excite other bound electrons. The initial free electrons gain energy through inverse bremsstrahlung heating from the electric field. Once the kinetic energy of these electrons is larger than the band gap, the excited electrons can collide with bound electrons giving the bound electrons enough energy to ionize. The change in the electron density is therefore linearly dependent on the electron density. Following the theoretical description of avalanche ionization in Shen [57], we set

$$R_{av} = \eta N \tag{3.66}$$

where η is the ionization rate for avalanche ionization. The ionization rate is directly proportional to the net absorption of energy by the electron. We implement a constant kinetic energy of the free electrons. We assume that an electron whose kinetic energy exceeds the ionization potential of the material immediately ionizes an electron. The kinetic energy is taken as the average kinetic energy of the electrons, $\frac{I_p}{2}$ [44]. In Shen et al [57], the avalanche ionization rate is given by

$$\eta = \frac{e^2|E|^2}{\Gamma m_e I_p(1 + \frac{\omega^2}{\Gamma^2})} \tag{3.67}$$

where e is the charge of an electron, m_e is the mass of an electron, I_p is the ionization potential of the material, E is the electric field, Γ is the electron-phonon collision frequency (as found in Eq. 3.43), ω is the optical frequency and $|E|^2$ is the magnitude of the electric field. The absorption of the electric field through inverse Bremsstrahlung heating is accounted for in the absorption due to the plasma (through the parameter Γ).

The diffusion of the electrons out of the ionization area and the recombination of electrons with ions occur at time scales much larger than the duration of a femtosecond laser pulse. Since, for this thesis, our simulations consider only femtosecond laser pulses, these processes are ignored here, however, they may be implemented in the future. As well, in the future, we can implement a routine that updates the collision frequency, and hence Γ, based on the electron energy, which would be updated through a rate equation for inverse Bremsstrahlung heating. However, for non-resonant systems, it is reasonable to implement a constant value for Γ.

Discrete Nonlinear Ionization Rate

In order to update our N value due to MPI and avalanche ionization, we must combine Eq. 3.39, Eq. 3.65 and Eq. 3.66:

$$\frac{dN}{dt} = \sigma I_e^6 + \eta N \tag{3.68}$$

Making this equation discrete, we find

$$N^{n+1} = \sigma\Delta t(I_e^{n+1/2})^6 + \frac{\Delta t e^2 |E^{n+\frac{1}{2}}|^2}{m_e I_p \Gamma(1+\frac{\omega^2}{\Gamma^2})} N^{n+\frac{1}{2}} + N^n \tag{3.69}$$

Simplifying this equation and substituting $N^{n+\frac{1}{2}} = \frac{N^{n+1}+N^n}{2}$ gives

$$N^{n+1} = \frac{1+\xi}{1-\xi} N^n + \Delta t\sigma(I_e^{n+\frac{1}{2}})^6 \tag{3.70}$$

where

$$\xi = \frac{\Delta t e^2 |E^{n+\frac{1}{2}}|^2}{m_e I_p \Gamma(1+\frac{\omega^2}{\Gamma^2})} \tag{3.71}$$

3.4.6 Complete Model

We now have a complete set of equations to model a material that exhibits linear properties as well as multiphoton ionization, avalanche ionization, dispersion due to plasma and nonlinear properties due to the optical Kerr effect. In addition, we have equations that model the electron density as a function of space and time. We need to now solve equation 3.38 for the electric field so that we can substitute this into update equations for the $\vec{H}$ field. From Eq. 3.38, 3.55, 3.60 and 3.64 we find

$$E^n = \frac{D^n - S_1^{n-1} + e^{-\Gamma\Delta t} S_2^{n-1}}{\epsilon_r + \frac{\omega_p^2 \Delta t}{\Gamma} - \frac{\omega_p^2 \Delta t}{\Gamma} e^{-\Gamma\Delta t} + \chi_{MPI}^{n-1} + \chi_{Kerr}^{n-1}} \tag{3.72}$$

Combining Eq. 3.72 with equations Eq. 3.51, Eq. 3.54, Eq. 3.70 and Eq. 3.59, we obtain the complete algorithm for modeling the medium. In general, χ_{MPI} and χ_{Kerr} are evaluated at time step n which requires E^n to be calculated through an iteration. However, for this thesis, we make the approximation that $\chi^n_{MPI} = \chi^{n-1}_{MPI}$ and $\chi^n_{Kerr} = \chi^{n-1}_{Kerr}$, which was found to be a reasonable approximation [26].

This FDTD code can be used to model numerous physical systems. It can model the propagation of various light sources through a nonlinear medium which exhibits multiphoton and avalanche ionization, plasma dispersion and Kerr nonlinearity as well as linear properties. By modifying the parameters, dielectrics with different nonlinear properties can be simulated. The parameters that need to be set in order to change the dielectric material simulated are the index of refraction (n_0), the nonlinear index of refraction (n_2) and the band gap (I_p). The number of photons absorbed to excite one electron may need to be changed as well. This will cause the cross-section of the multiphoton interaction (σ) and the order of the interaction to change. Different experimental set-ups can be modeled by integrating different materials in the simulation space through the use of an input file. The different materials could be anything from a vacuum-fused silica interface to a material that has been ionized previously in a specific pattern. These modifications are straight-forward allowing this code to be quite verstile.

As well as different materials and geometries, this code can simulate various sources. In general, experiments are done with a pulsed, focused laser. This can be simulated by a Gaussian source in space and time. However, this could be extended as shown above to model more tightly focussed beams. In addition, a plane wave source can be useful for approximating the field in a small area. Light sources that have not been described in this chapter could easily be added to this code by introducing the functional form of that source as a hard or soft source.

In the next chapter, we discuss the initial results obtained with the code. We investigate the interaction of a pulsed, Gaussian beam source with fused silica.

Chapter 4

Nonlinear Ionization in Fused Silica: FDTD Simulations

Using the model introduced in Chapter 3, we perform three-dimensional simulations thereby giving a deeper understanding of the physical mechanisms in nonlinear ionization of dielectrics. These simulations are in three space dimensions plus one dimension for time and calculate the electric and magnetic fields as well as the electron density at every point in space and time. In this chapter, we investigate the results of our FDTD simulations. First, we introduce simple test scenarios in order to determine the accuracy of our models for the multiphoton absorption, the plasma dispersion and the Kerr effect. We then investigate the shape and density of the region ionized by a focused ultrashort laser beam. The results are then analyzed in the planes parallel and perpendicular to propagation. We then plot the electric field and electron density at different time steps to determine the growth of the region over time.

4.1 Evaluation of Model

In the following section, we investigate the simulation's ability to predict the correct results for the processes added to the basic FDTD algorithm in Chapter 3.

4.1.1 Multiphoton Absorption

To test our model of mulitphoton absorption, we compare it to experimental results and the self-limiting absorption model introduced by Rayner et al [50]. As discussed in Section 1.4, Rayner et al [50] hypothesize that the intensity is cut at a measurable threshold due to multiphoton absorption. We simulate this by introducing a pulsed, plane wave (Section 3.2.1) into fused silica which, because of its symmetry and simplicity, gives a clear view of the effect of the absorption. In this simulation, we used a Gaussian envelope in time with a plane wave soft source. The FWHM of the pulse was $12fs$ with maximum intensities of $I = 2.25 \times 10^{13} \frac{W}{cm^2}$ and $2.8 \times 10^{13} \frac{W}{cm^2}$ in fused silica. These intensities were chosen because they are well over the experimentally determined threshold intensity of $1.5 \times 10^{13} \frac{W}{cm^2}$ [23].

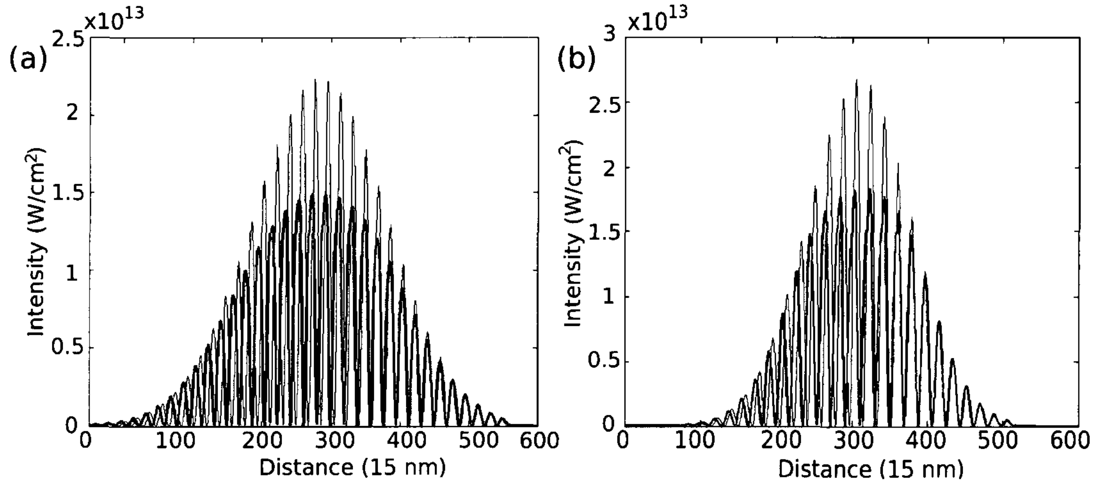

Figure 4.1: *Gaussian pulse in time. (a) Blue curve shows intensity in linear dielectric, green curve shows intensity in nonlinear medium. (b) Blue curve shows intensity in linear dielectric, red curve shows intensity in nonlinear medium.*

In Fig. 4.1, we have plotted the intensity along the propagation direction. For comparison, we have also plotted the intensity in a dielectric that has the same refractive index as fused silica but does not exhibit any nonlinear effects. In Fig. 4.1(a), we see that the intensity in fused silica with nonlinear effects reaches a peak of $1.5 \times 10^{13} \frac{W}{cm^2}$. The intensity in the simulation with no nonlinear effects reaches a peak of $2.25 \times 10^{13} \frac{W}{cm^2}$. The cut-off for the intensity agrees well with the threshold intensity measured by experiment ($1.5 \times 10^{13} \frac{W}{cm^2}$ [23]).

However, when we increase the peak intensity, the cut-off threshold increases. In Fig. 4.1(b), the maximum intensity was $2.8 \times 10^{13}\frac{W}{cm^2}$ and the threshold was $1.85 \times 10^{13}\frac{W}{cm^2}$. This value, though different from the measured value, is within experimental uncertainty. The absorption due to multiphoton ionization does in fact limit the intensity inside the dielectric however it is dependent on the peak intensity of the source. We see a curved peak, similar to the Gaussian profile of the incident beam, instead of a straight, flat cut in intensity as hypothesized. As our model of multiphoton absorption agrees well with both the experimentally determined threshold intensity and the self-limited absorption model, we will use this model to determine if this capped intensity may be the cause of the shape created by pulsed focused lasers as noted in Rayner et al [50] by simulating a pulsed, focused source.

4.1.2 Drude Model of Plasma

To test our implementation of a Drude medium, we performed a simulation in which a Gaussian pulse in time was incident on a plasma half space. This simulation was used to test the model because an analytical solution for this scenario exists. The reflected and incident waves were Fourier transformed into frequency space to determine the reflection coefficient as a function of frequency as seen in Fig. 4.2. We compare the FDTD calculation with the

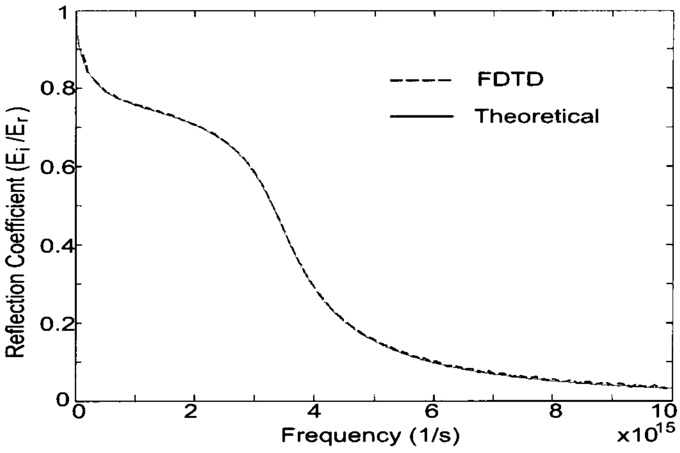

Figure 4.2: *Reflection coefficient of a plane wave incident on a plasma half-space.*

analytic form of the reflection coefficient given in Barnes et al [2]

$$R = \frac{n - \tilde{\epsilon}(\omega)^{1/2}}{n + \tilde{\epsilon}(\omega)^{1/2}} \tag{4.1}$$

$$\tilde{\epsilon}(\omega) = 1 - \frac{w_p^2}{\omega - i\omega^2\Gamma} \tag{4.2}$$

where R is the reflection coefficient, w_p is the plasma frequency, Γ is the collision frequency and n is the index of refraction of the dielectric half-space. As can be seen in Fig. 4.2, the FDTD calculation agrees well with the theory.

4.1.3 Kerr Nonlinearity

To demonstrate the extent of self-focusing due to the Kerr nonlinearity, a focused Gaussian beam is propagated through a dielectric which only exhibits the Kerr nonlinearity with $n_2 = 2 \times 10^{-16}\frac{cm^2}{W}$. We use a continuous source, propagating from the left, so that a complete picture of the focusing is visible at a single time step. In the Kerr medium (Fig. 4.3), it can be seen that the beam exhibits self-focusing and continues to focus after the Gaussian focal position of $z = 10000nm$. In Fig. 4.3(a), the electric field for a Gaussian beam propagating in a Kerr medium is plotted. The same parameters are used in the simulation in a medium which only exhibits linear properties. The electric field in the dielectric medium is subtracted from the electric field in the Kerr medium. This difference is plotted in Fig. 4.3(b). We look at the difference between the two so that the extent of self-focusing is easier to see. The difference is mainly after the focus of the Gaussian beam, once the beam has reached its maximum intensity, and is comparable in magnitude to intensity of the beam. We see from the difference that the electric field is increased in the Kerr medium close to the focus and the difference continues to increase as the field propagates. This shows that as the beam focuses and the intensity increases, the self-focusing effect of the Kerr nonlinearity is more predominant. This agrees with the expected behaviour of a Gaussian beam in a medium with an appreciable n_2 factor.

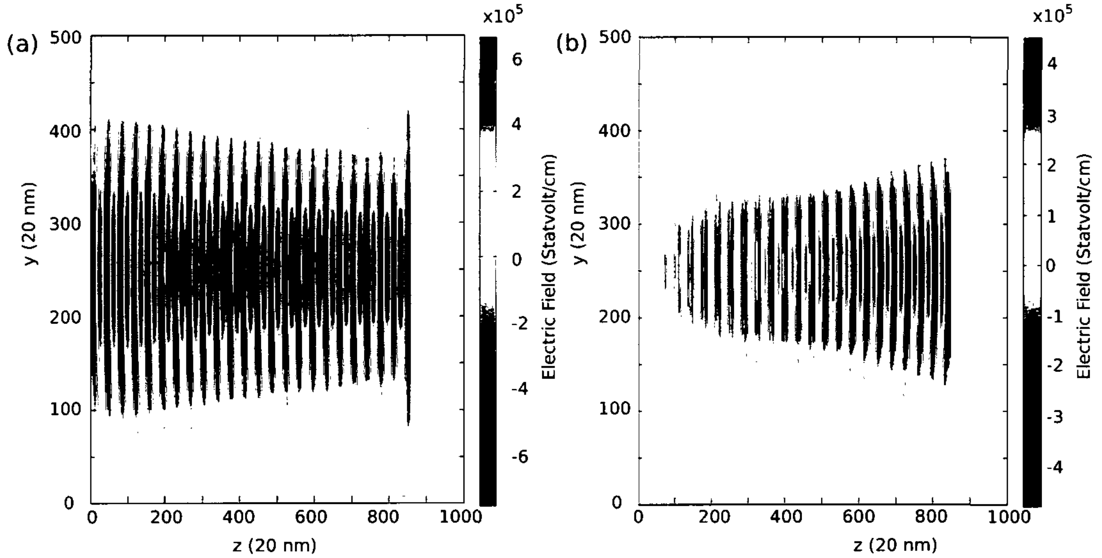

Figure 4.3: *Electric field focused Gaussian beam in (a) Kerr medium and (b) the difference between the electric field in the Kerr medium and in a nonlinear dielectric*

4.2 Formation and Properties of the Modified Region

Now that we have determined that our model predicts the correct results, we investigate the formation of the modified region by simulating an ultrashort laser pulse focused into fused silica. This is similar to the experiments done on this subject [22]. To determine the relative importance of plasma dispersion, self-focusing via the Kerr effect, and multiphoton absorption we performed simulations with and without each process. We are able to see the effect these processes have on the shape and electron density of the modified region. Since the modified FDTD code used for these simulations is incremented over time, we are able to observe the growth of this region over the duration of a pulse. This is difficult to observe in experiment. A look at both the electric fields and the electron density will give insight into how the region forms.

In the following simulations, we model fused silica interacting with various intense light sources. Fused silica is modeled with an ionization potential of $I_p = 9eV$ while the incident light has a central wavelength of $\lambda = 800nm$. This means that the ionization process will involve six photons. Avalanche ionization was not used in these simulations because the pulse duration is too small for any appreciable ionization due to this effect [52]. Fused silica has a refractive index of $n = 1.453$ and a six-photon cross-section of $\sigma = 2.1 \times 10^{-47} \frac{cm^9}{sW^6}$ [7]. The relaxation time was taken as $\tau = 1fs$ [44] and the Kerr nonlinearity was characterized by $n_2 = 2 \times 10^{-16} \frac{cm^2}{W}$ [23].

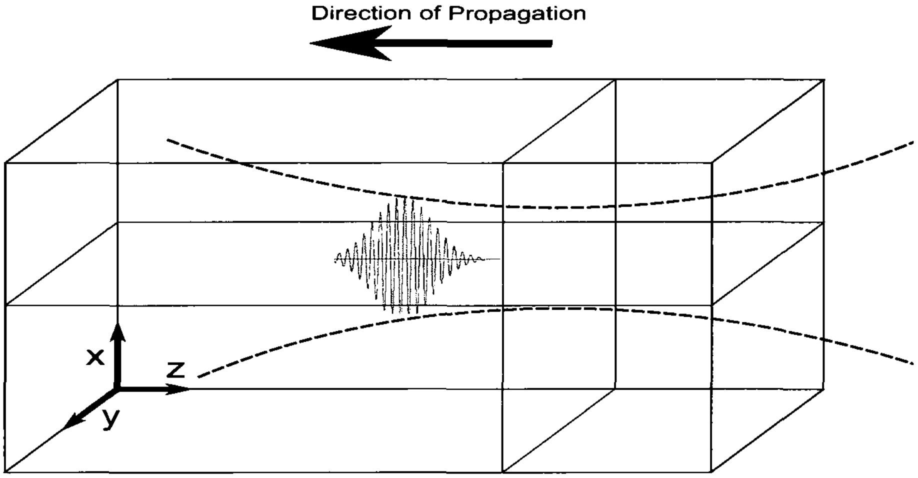

Figure 4.4: *Simulation space with incident laser beam. The blue rectangles represent the perpendicular and parallel planes that are investigated in this chapter.*

For our simulations we used a spatial step of $\Delta x = \Delta y = \Delta z = 20nm$ and a time step of $\Delta t = 3.33 \times 10^{-17}s$. This grid size limits our resolution however this is the smallest size possible that allows for the electric field to be zero at the boundaries with our current computer resources. To simulate an ultrashort laser pulse focused into fused silica, we used a hard source with a Gaussian profile in space and time (Section 3.2.2). We used a beam width of $w_0 = 1.5\mu m$ with the focus at $z = 375$. This causes the beam to focus in the centre of the simulation space with sufficient space before the focus for carrot formation. Some reflections are created due to the plasma, however, the distance between the beginning of the simulation space and the peak electron density is large enough that these do not play an important role. The width of the Gaussian beam was chosen because it is simular to the focus used in experiment but also allows for a small simulation space. The pulse is propagated from the right side of the simulation space. The FWHM of the pulse was $\Delta t = 1.67 \times 10^{-14}s$. The polarization of the source is parallel to the $y - z$ plane. The intensities were chosen such that carrot formation was observable while the electron density remains below the saturation limit of fused silica. The coordinates of the simulation space are shown in Fig. 4.4 with respect to the laser propagation. In the next sections we will investigate the intensity dependence of the modified region and the morphology in the plane parallel $(y - z)$ and the plane perpendicular $(x - y)$ to the propagation direction.

4.2.1 Parallel Plane Morphology

In this section, we look at the morphology of the modified region in the plane parallel to the propagation direction of the laser beam. The simulation was run with an intensity of $8.2 \times 10^{13}\frac{W}{cm^2}$ to examine the different effects of each process. After the laser pulse interacts with a medium which contains all processes, at $9.99 \times 10^{-14}s$, the electron density is plotted in Fig. 4.5(a). We see the region of high electron density has the same shape as the modified region seen in experiment. In general, we find that the carrot is formed before the focus. As discussed later in this section, this location depends on the initial intensity, however, the peak is before the focus for all intensities where a clearly defined carrot shape can be observed. This is mainly caused by the absorption associated with the multiphoton ionization which depletes the beam.

It is not clear what causes the shape of the plasma. One theory is that the shape arises from the depletion of the beam due to multiphoton ionization [50]. Another theory states that the shape arises from the light forming a spatial soliton because of the balance between plasma dispersion and self-focusing due to the Kerr effect [9].

In Fig. 4.5, a slice of the electron densities are plotted through the middle of the modified region in the $y - z$ plane. Fig. 4.5(a) shows the electron density when all processes are present while in Fig. 4.5(b) the Kerr effect is removed, in Fig. 4.5(c) the plasma dispersion is removed and in Fig. 4.5(d) the multiphoton absorption is removed. It is important to note that while

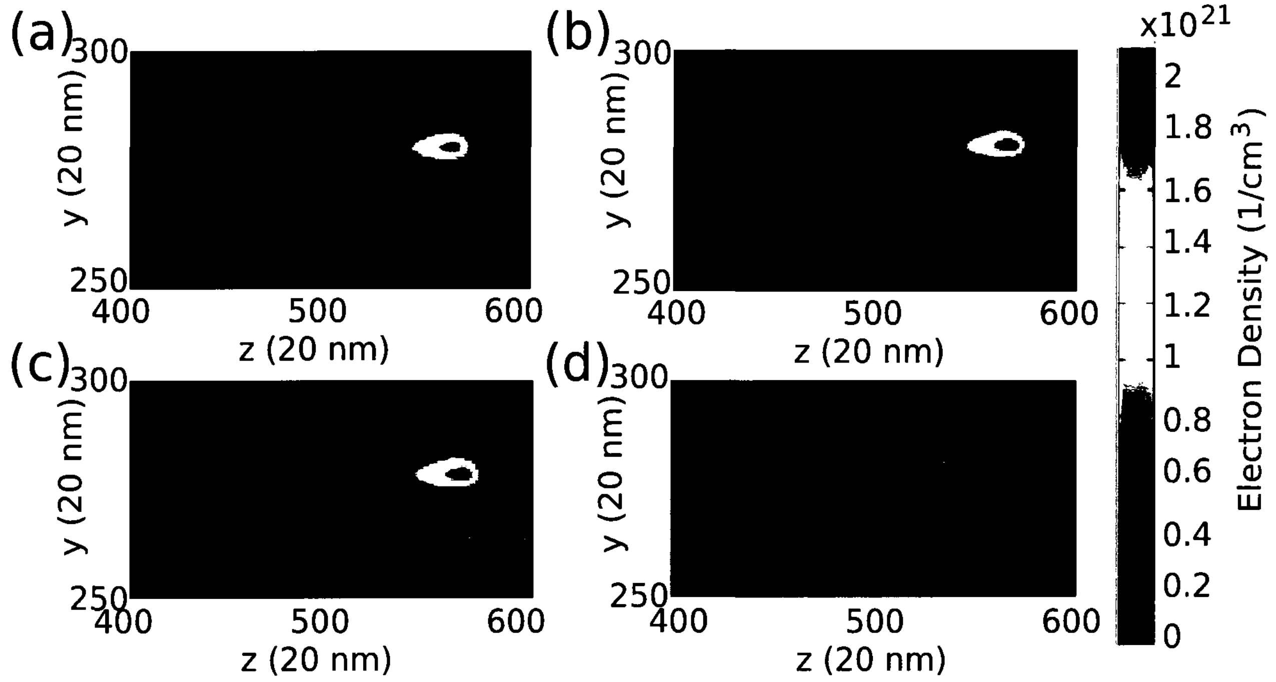

Figure 4.5: *The electron density for simulations run with (a) all processes present, (b) Kerr effect absent, (c) plasma dispersion absent, (d) multiphoton absorption absent.*

the absorption of the electric field due to multiphoton absorption is removed, multiphoton ionization is still implemented to increase the electron density. It is immediately obvious that the largest change in the electron density occurs when the multiphoton absorption is removed. Although the regions in the simulations without the Kerr effect and plasma dispersion are slightly different in position or peak electron density, the shape of the region remains very similar to that of the simulation run with all processes present. Without the multiphoton absorption, the distinct carrot-shape is not present at all. We will investigate each of the plots in more detail.

Plasma Effects

In Fig. 4.5(c), the plasma effects were removed. A plot of the difference between the simulation run with plasma dispersion (Fig. 4.5(a)) and without plasma dispersion (Fig. 4.5(c)), $N_{withoutplasma} - N_{withplasma}$, is plotted in Fig. 4.6. As we see, the electron density is higher in the case without the plasma. The largest differences are in the areas of highest electron density. This is due to metallic properties of the plasma which cause exponential decay of the field inside the plasma. Without this decay, there would be a larger intensity in the ionized region allowing for more ionization. In the simulation without the plasma dispersion, the higher ionization rate at the top of the region depletes the field slightly more than the simulation with the plasma dispersion immediately after this region. This creates a lower electron density immediately after the peak. As well, the beam would no longer experience defocusing due to dispersion. It is also notable that the electron density retains the same shape with or without the plasma effects.

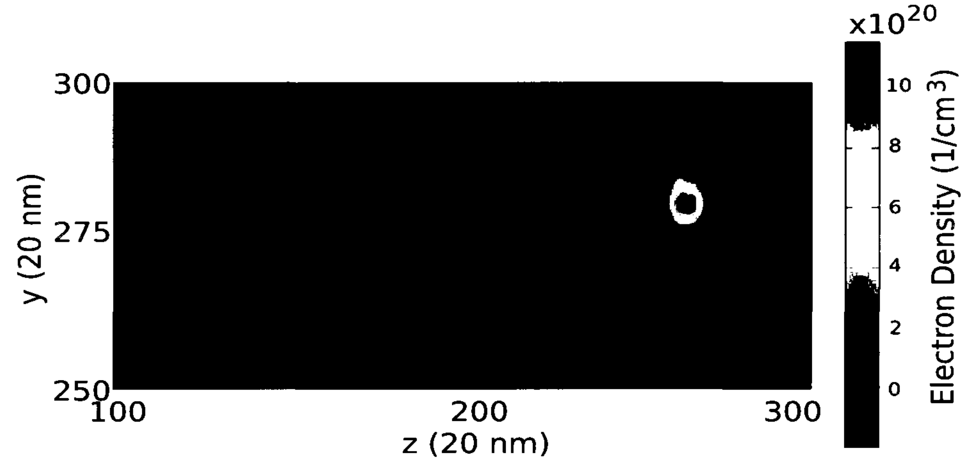

Figure 4.6: *Difference between simulation run with plasma dispersion and without for* $I = 8.2 \times 10^{13} \frac{W}{cm^2}$. *The focus of the beam is located at* $z = 375$.

Kerr Nonlinearity

We observe the effect the Kerr nonlinearity has on the electron density in Fig. 4.5(b). The peak electron density is moved towards the source when the simulation is run without the Kerr effect. This is an interesting result as it is counter-intuitive. One would expect that the self-focusing caused by the Kerr effect would create the modified region to occur earlier, not later as observed. In Fig. 4.7, a line through the centre of the modified region is plotted for various intensities. It is interesting to note that for $I = 7.3 \times 10^{13}$, there is no difference between the electron density created with the Kerr effect and that created without. As we can see, the position of the peak electron density is closer to the focus when the Kerr effect is present for all intensities. This may be because, as the beam is self-focused by the Kerr effect, more ionization occurs earlier. This then causes more energy loss of the field because there is more ionization to cause multiphoton absorption. The intensity would then not be high enough to create the highly ionized peak until closer to the focus. This would also explain the decreased peak seen with the Kerr effect. However, the reasons for this effect are not immediately obvious and require further investigation.

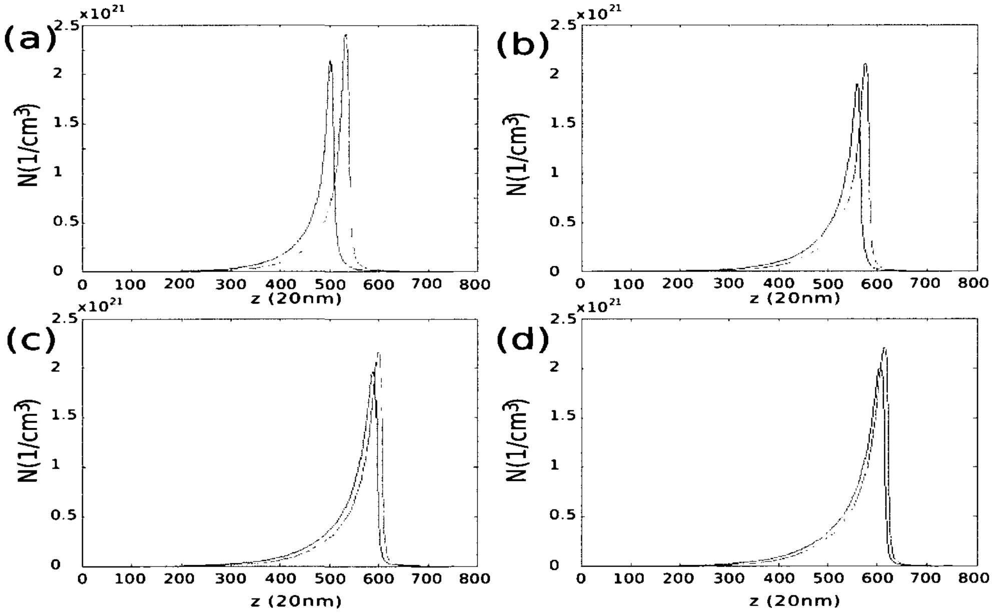

Figure 4.7: *A slice through the centre of the carrot along the direction of propagation at (a)* $I = 7.7 \times 10^{13}$*, (b)* $I = 8.2 \times 10^{13}$*, (c)* $I = 8.6 \times 10^{13}$*, (d)* $I = 9 \times 10^{13}$*. The blue line represents the simulation with the Kerr effect and the green line represents the simulation without the Kerr effect.*

The Kerr effect also increases the electron density after the peak. This results in a lengthened carrot shape when the Kerr effect is present. This effect is less significant than Fig. 4.3 would suggest though it is still present. This is due to the increased threshold mentioned in Section 4.1.1. With the higher threshold, the Kerr effect is stronger, increasing the amount of ionization after the focus. However, it is still limited since the region beyond the focus has a significantly lower electron density than the top of the modified region. It is clear from Fig. 4.5(b) the modified region created without the Kerr nonlinearity still exhibits an elongated shape. Thus the shape cannot be entirely caused by the Kerr nonlinearity.

Multiphoton Absorption Effects

If we look at the plot in Fig. 4.5(d) on a more appropriate scale, it is clear that the ionized region is significantly different (Fig. 4.8). The region is less confined. The region directly after the source experiences significantly more ionization since multiphoton absorption is not present and therefore there is unlimited energy for ionization. The only loss in energy of the field is through the metallic properties of the plasma which cause an exponential decay as the light propagates through the plasma. Because the ionization rate is highly dependent on intensity, the exponential decay of the field gives the decaying plasma that is seen in Fig. 4.8. This effect is exaggerated because of the abnormally high electron density near the source. The focus of the beam can be seen through the tapering of the ionized region. However, by the time the beam has reached the focus, it is not intense enough to create significant ionization because of the exponential decay due to the plasma. If the multiphoton absorption was present, the ionization close to the source would be limited and the exponential decay due to the plasma formed would be less.

From Fig. 4.5 and Fig. 4.8, it is clear that the depletion of the laser beam is indeed the source of distinct shape. The depletion of the beam limits the ionization close to the source allowing the beam to propagate into the material. Because the beam can propagate further, it focuses creating a more confined modified region. The peak ionization is seen as soon as the electric field reaches a threshold intensity. The subsequent ionization depletes the beam causing the modified region to taper off. This implies that the primary cause of the particular shape of the region is self-limiting absorption.

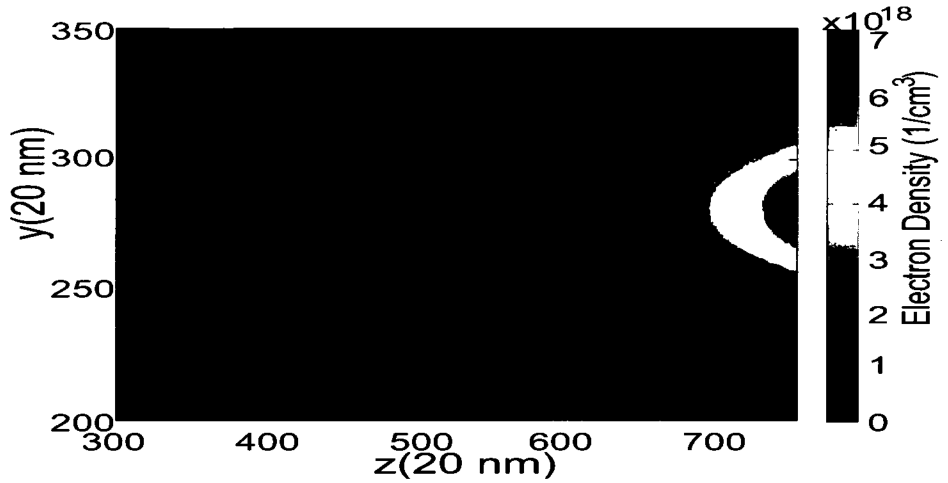

Figure 4.8: *The electron density for simulation without multiphoton absorption.*

Intensity Dependence

To determine the intensity dependence of the modified region, the laser pulse was initiated with intensities at the focus in vacuum ranging from $7.3 \times 10^{13} \frac{W}{cm^2}$ to $9 \times 10^{13} \frac{W}{cm^2}$. A cut through the centre of the modified region in the $y-z$ plane is shown in Fig. 4.9 for each simulated intensity. The scale is the same for all plots. It is notable that below $I = 7.5 \times 10^{13} \frac{W}{cm^2}$, there is no notable ionization or carrot formation. In this case, the largest electron density seen is approximately $9 \times 10^{18} \frac{1}{cm^3}$, more than two orders of magnitude smaller than the electron density when $I = 9 \times 10^{13} \frac{W}{cm^2}$. It is also notable that there is a large discrepency between the $I = 7.3 \times 10^{13} \frac{W}{cm^2}$ and the $I = 7.5 \times 10^{13} \frac{W}{cm^2}$ simulations. After this jump, there is very little change in the electron densities of the larger intensity simulations. Since ionization is a highly nonlinear process, the electron density is highly dependent on intensity. A small increase in intensity can have a large effect on the electron density. This explains the large difference between Fig. 4.9(a) and 4.9(b). This effect is known as a threshold intensity for nonlinear ionization. However, once the intensity increases past the threshold, the beam becomes depleted due to multiphoton absorption. Instead of an increase in peak electron density, the large-scale ionization occurs closer to the source creating a longer modified region. Thus though the total electron density increases with increasing intensity, the peak electron density does not continue to increase at the rate it did at lower intensities.

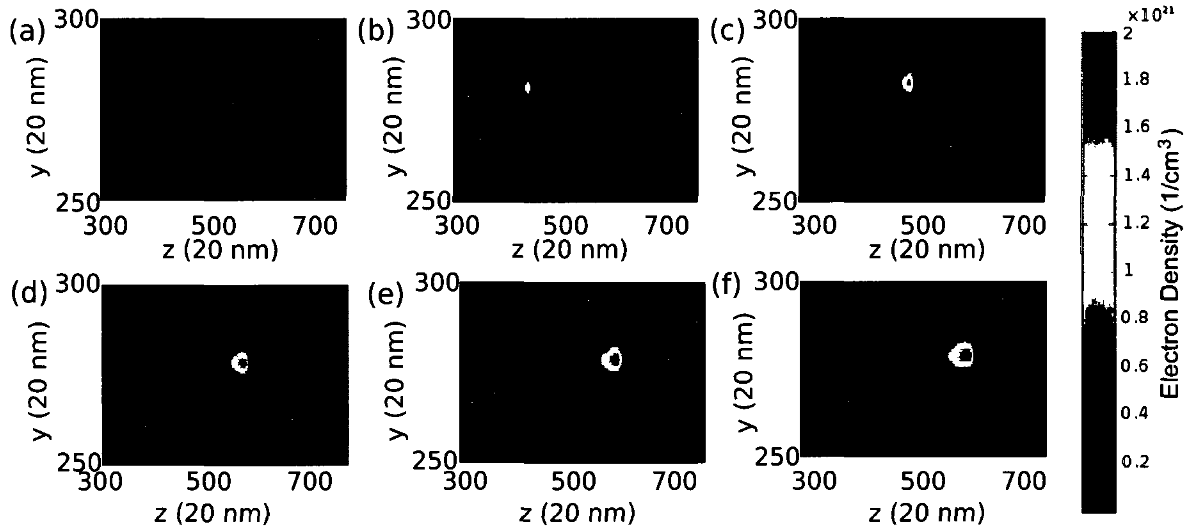

Figure 4.9: *Electron density with initial intensities of (a)* $7.3 \times 10^{13}\frac{W}{cm^2}$, *(b)* $7.5 \times 10^{13}\frac{W}{cm^2}$, *(c)* $7.7 \times 10^{13}\frac{W}{cm^2}$ *(d)* $8.2 \times 10^{13}\frac{W}{cm^2}$, *(e)* $8.6 \times 10^{13}\frac{W}{cm^2}$, *(f)* $9 \times 10^{13}\frac{W}{cm^2}$

As the intensity is increased above the threshold, the shape and location of the modified region changes more than the peak electron density. As the intensity is increased, the top of the modified region moves towards the source (away from the focus). As well, the region becomes more elongated with larger intensity. As the beam focuses, the intensity increases. In each case, at a certain point, the intensity reaches a value above the threshold of the material. At this point, large scale ionization occurs and the top of the modified region appears. For a larger initial intensity, the threshold intensity will be reached sooner therefore moving the top of the modified region closer to the source. Since the intensity is larger throughout the entire pulse, there is a longer region where ionization can sill occur. This will cause the elongation of the modified region.

The intensity that first produces a notable carrot shape does not correspond exactly to the multiphoton absorption threshold mentioned in Section 4.1.1. This is because the intensity is measured at the focus of the beam and so before the focus the intensity is lower than stated. For intensities below the carrot forming threshold, multiphoton ionization occurs however, it occurs close to the focus and does not possess a carrot shape. For the carrot-shape to form, the intensity must be high enough before the focus to produce a large amount of ionization.

4.2.2 Perpendicular Plane Morphology

As the FDTD model used in this study is three-dimensional, we investigate the morphology in the plane perpendicular to the direction of propagation. If we take a slice in this direction at the peak of the electron density after the pulse, we see that the modified region is elliptical opposed to circular as assumed by most numerical studies of this system (Fig. 4.10(a)). This effect is shown in Simotsuma et al [58] as seen in Fig. 4.10(b). As we move away from the peak electron density, the ellipticity decreases. Near the focus of the beam, the profile of the modified region in the $x - y$ plane is circular (Fig. 4.10(c)). These tiny circles are currently studied experimentally.

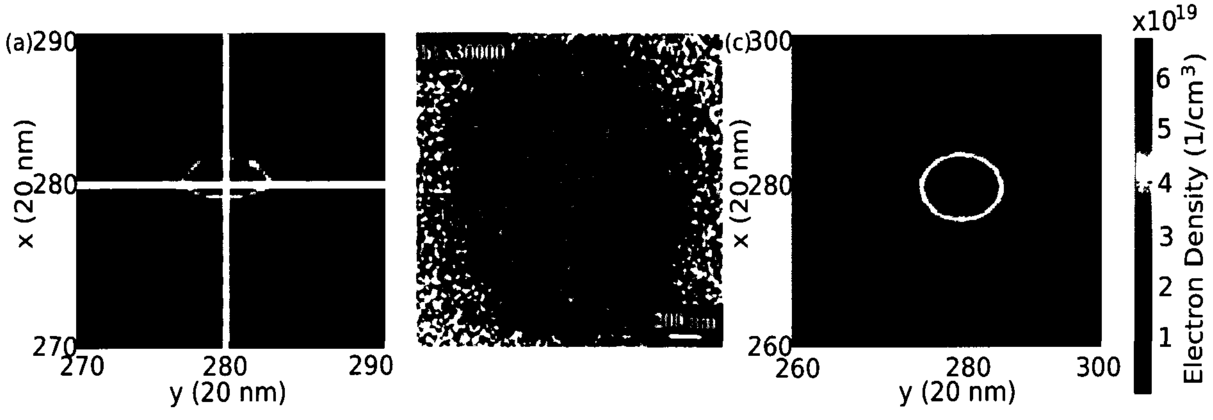

Figure 4.10: *(a) Electron density through the peak of the modified region. White lines represent cuts through the region parallel and perpendicular to the polarization direction. The electric field is polarized in the x-direction. (b)Picture of damaged material from experiment. The electric field is polarized in the y-direction. (c) Electron density through the location of the laser focus with* $I = 8.2 \times 10^{13}$.

The flattening of the modified region is polarization dependent; the widest part of the ellipse corresponds with the direction of polarization. It is interesting to note that if we assumed that the modified region was an oval, the local fields due to the plasma as discussed in Rajeev

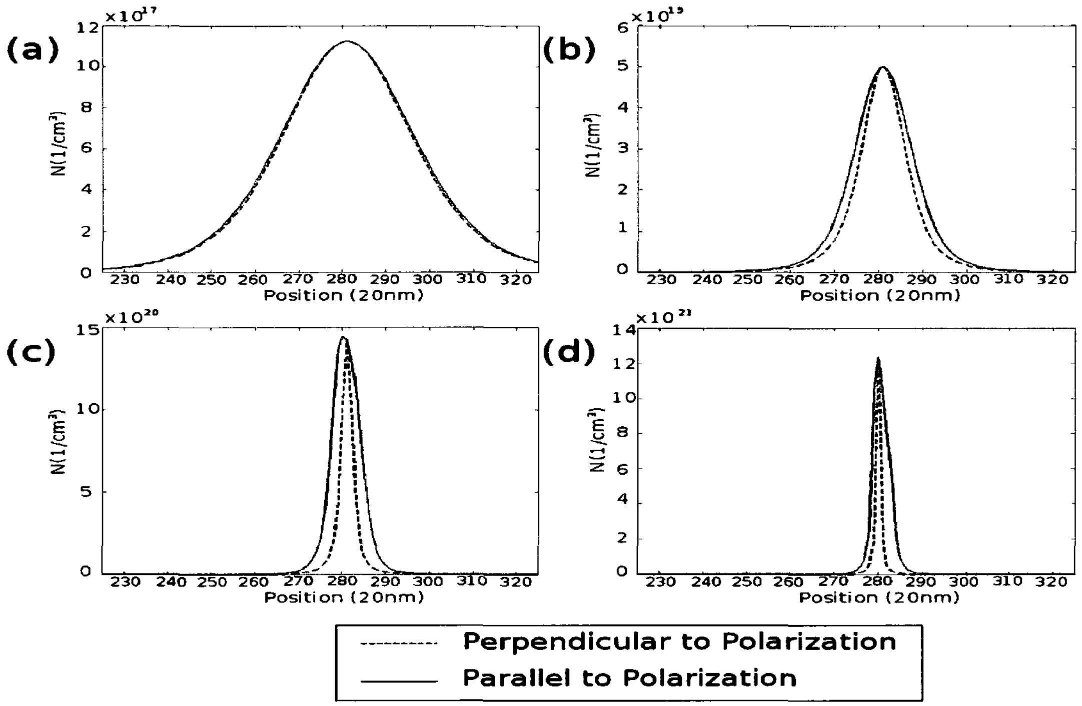

Figure 4.11: *Electron density through the centre of the modified region parallel and perpendicular to the polarization at time (a)* $t = 1100\Delta t$, *(b)* $t = 1300\Delta t$, *(c)* $t = 1550\Delta t$ *(d)* $t = 1700\Delta t$ *with* $I = 8.2 \times 10^{13}$

et al [48] and Section 1.5.2 would cause the modified region to be flattened in the opposite direction than what is observed. As we see in Fig. 4.11, the ratio of the larger radius to the smaller radius increases in time. In simulations run without the plasma effects, this flattening of the modified region is still present which implies that plasma effects cannot play a role in the ellipticity. The effect must be caused by multiphoton absorption. We therefore take a closer look at the field distribution. For a focus with a radius of $1.5\mu m$, the longitudinal component of the electric field is approximately 10% of the peak of the electric field. This field is signficant enough to cause an increased ionization. A contour plot of the E_z component at the peak electron density location is shown in Fig. 4.12 for the linear dielectric case. The z-component has a peak along the polarization direction and a minimum along the direction perpendicular to the polarization. This distribution corresponds to the ellipticity seen in the electron density. It is clear that the ellipticity is caused by the tight focusing of the laser beam.

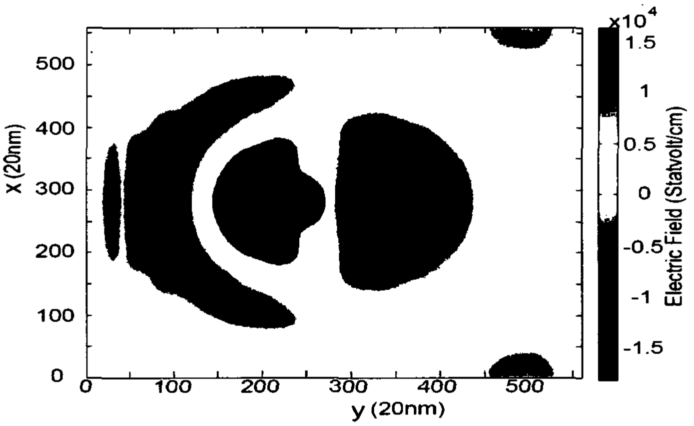

Figure 4.12: *Longitudinal component of the electric field through the peak of the modified region. The electric field is polarized in the y-direction.*

4.2.3 Time Evolution

With the modified FDTD code, the electric field and electron density can be outputted for each point at every time step. Therefore, we can observe the growth of the modified region over time. We have plotted the electron density and electric field at various times in Fig. 4.13 and Fig. 4.14. In these plots, the focus is at $z = 75$.

At the first time step shown, the centre of the pulse has just passed through the peak of the modified region creating the first appreciable sign of ionization. This ionization creates a bend in the electric field as the field is absorbed due to the ionization. When the simulation is run without plasma effects, the distortion of the field seen in Fig. 4.14 is still present. Therefore, the distortion is caused entirely by multiphoton absorption.

We see from Fig. 4.13 and 4.14, that the portion of the field that is slightly bent away from the focus corresponds to high ionization rates. In Fig. 4.15, we look at an early time step in detail. The ridges seen in Fig. 4.15(b) correspond directly with the lagging peaks in the electric field and are $\frac{\lambda}{2n}$ apart. In the simulations run without plasma effects, the ridges were still present implying that they are caused by multiphoton absorption. To observe the direct cause of the ridges, we made a movie depicting the electric field and the electron density over

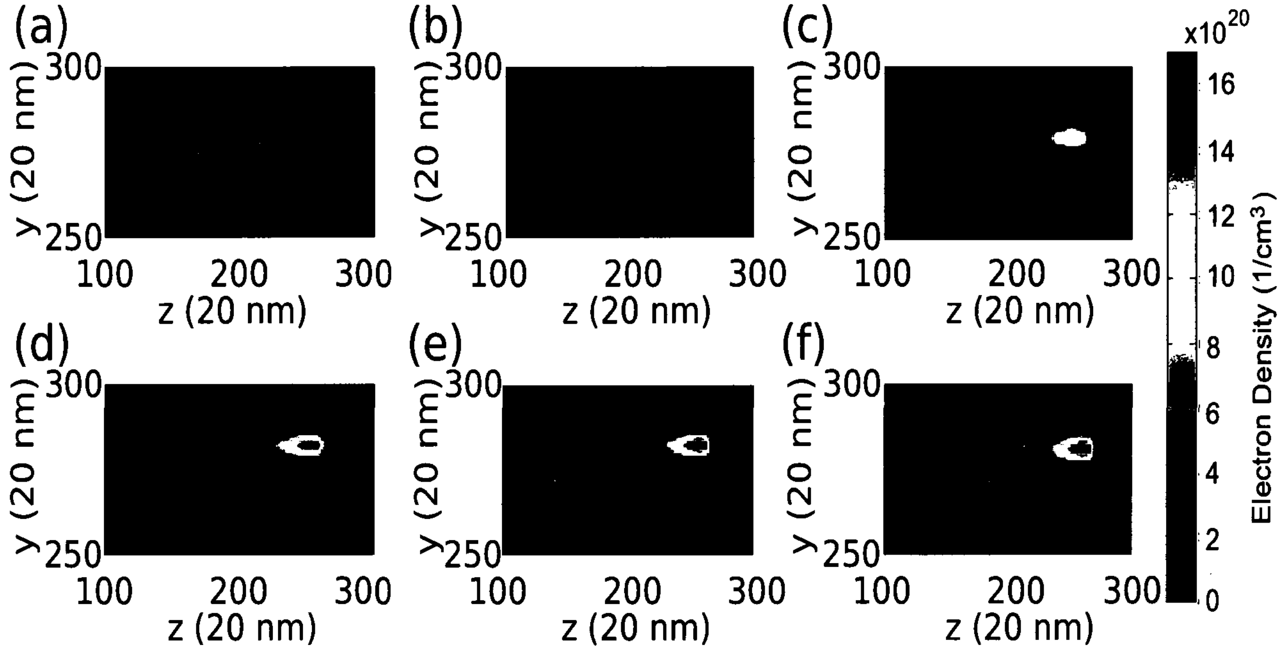

Figure 4.13: *Electron density at (a)* $t = 1350\Delta t$*, (b)* $t = 1450\Delta t$*, (c)* $t = 1500\Delta t$ *(d)* $t = 1550\Delta t$*, (e)* $t = 1600\Delta t$*, (f)* $t = 1800\Delta t$ *with* $I = 8.2 \times 10^{13}$

time. We found that the ridges moved with the peaks of the electric field and thus are caused by a sub-cycle self-limited absorption. At the beginning of the pulse, the sub-cycle peaks of the electric field increase in time. At a certain point, the sub-cycle peak will be higher than the threshold intensity. The electron density will then increase significantly while the field is above the threshold creating the ridges seen. The effect of this on the electric field is seen in the bending of the field (Fig. 4.15(a)). These ridges are smoothed out as the field increases so that it is above the threshold for longer periods as the pulse propagates through the region.

4.3 Summary of Results

Through numerous simulations using the modified FDTD code introduced in Chapter 3, a great deal was discovered regarding the formation of the modified region. Since our model

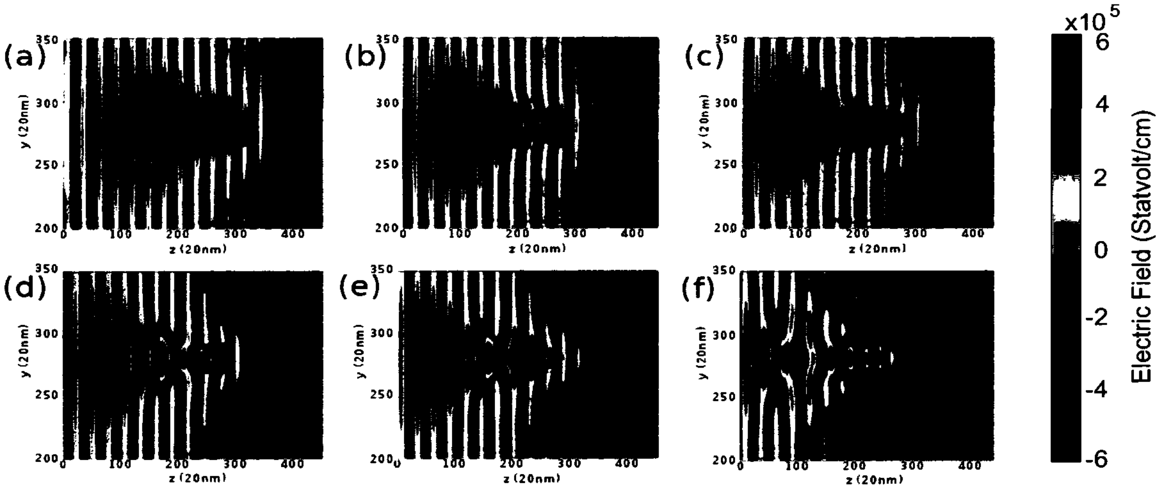

Figure 4.14: *Electric field at (a)* $t = 1350\Delta t$*, (b)* $t = 1450\Delta t$*, (c)* $t = 1500\Delta t$ *(d)* $t = 1550\Delta t$*, (e)* $t = 1600\Delta t$*, (f)* $t = 1800\Delta t$ *with* $I = 8.2 \times 10^{13}$

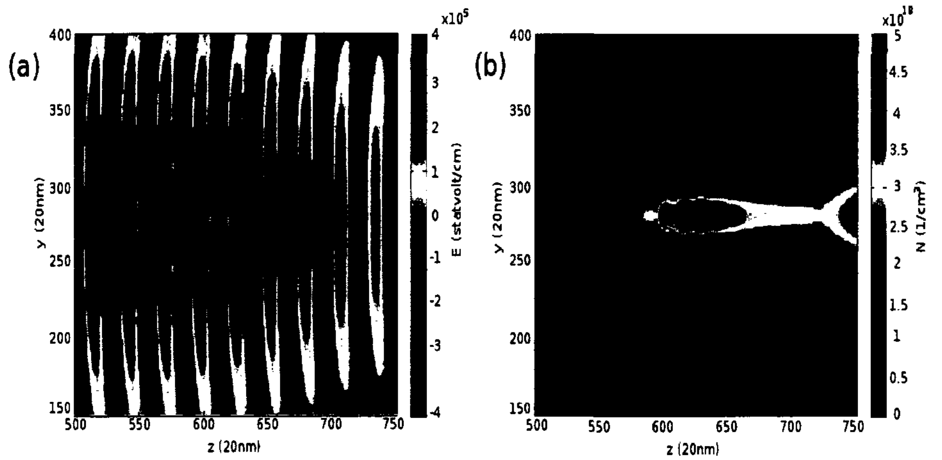

Figure 4.15: *(a) Electric field and (b) Electron Density at* $t = 1000\Delta t$ *with intensity* 8.2×10^{13}*. The arrow indicates a distance of* $\frac{\lambda}{n}$*.*

predicts the correct results in simple test scenarios, we used it to simulate a femtosecond laser focused inside fused silica. We found that the omission of plasma effects and the Kerr nonlinearity only result in a somewhat higher electron density at the peak and a shift in the peak of the electron density, respectively. It is notable, however, that the electron density retains the same carrot-like shape in the propagation direction, and the same asymmetric (perpendicular) cross section when plasma and Kerr effects are neglected. By changing the initial intensity, the position of the peak ionization can be moved away from the focus. We determined that the carrot shape becomes apparent at an intensity of 7.5×10^{13}. We observed periodic ridges formed at the beginning of the ionization which were caused by the multiphoton absorption. Thus we find that the morphology of laser damage is predominantly caused by the self-limiting effect of multiphoton absorption.

Chapter 5

Conclusion

This thesis has investigated the interaction of an intense, ultrashort laser pulse with fused silica. Previous experiments had shown that this interaction produces a confined change in refractive index inside the glass. The formation of the region is not well understood. High intensity interactions with dense mediums such as solids are difficult to investigate analytically because of the numerous complicated processes that are important. Aspects of the modified regions, such as the subwavelength nanocracks, were unexpected and emphasize the need for a better understanding of the processes that create the modified regions.

We employed two methods to investigate these systems: through an analytical look at the spacing of the nanocracks and through computational simulations of the ionization. For the former, we started from a theory from Rajeev et al [48], assuming that the spacing arose from small nanoplanes behaving as parallel plate waveguides. We found that, according to this theory, the minimum spacing decreased with decreasing plasma frequency. For high plasma frequency, or a metal-like plasma, the spacing approached $\frac{\lambda}{2n}$ as is expected from the perfectly conducting waveguide model. However, this theory neglected the electric field components of the TM modes. Since the peak of electric field is maximal in the centre of the waveguide, it is unclear how nonlinear ionization would be affected.

The main contribution of this thesis is the development and use of the extended Finite-

Difference Time-Domain method. The FDTD method for calculating electric and magnetic fields has been used to simulate the linear interactions since 1966. However, in order to simulate intense, ultrafast laser interaction with dielectrics, an extension that incorporated nonlinear interactions and plasma effects was necessary. This thesis introduced a protocol to simulate multiphoton ionization, avalanche ionization, plasma dispersion and the nonlinear Kerr effect, and a rate equation describing the growth of the electron plasma.

The extended FDTD code was used to investigate the modified region observed in experiment. We found that the region formed into a carrot shape, agreeing with experimental observations. The peak intensity was found in the top portion of the carrot and the carrot formed before the focus of the laser beam was reached. The position of this peak depended on the intensity of the source — the more intense the source, the farther the peak was from the focus. Further, we were able to observe a threshold for carrot formation. By looking at the electron density and field profiles as a function of time, we were also able to observe the formation of the modified region as a movie. In the early stages of formation, there were periodic ridges in the electron density. This was seen to arise from sub-cycle multiphoton absorption. When we looked at the electron plasma in cross-section perpendicular to the propagation direction, we observed that the plasma region was ellipitical. We found that this is due to tight focusing which creates a significant longitudinal field along the y axis; the intensity of this eld reaches 10% of the peak. By eliminating from the simulation each physical process one at a time, we were able to determine that multiphoton absorption was the cause of the distinct shape of the ionized region. The shape of the modified region agrees well with those seen in experiment. This consistency is one verification of the modified FDTD code used in this study.

The code developed in this thesis is a powerful new tool applicable to many other outstanding problems in intense laser-matter interaction. For example, it could be used to investigate why and how the subwavelength periodic nanocracks are formed. In particular, we could investigate Rajeev et al's [48] theory that the nanocracks arise from small plasma balls that elongate in the electric field to create planes. This could be accomplished, for example, by incorporating a non-zero electron density in the shape of a sphere in the centre of the simulation space at the beginning of the simultion. The results from the previous simulations show that small increases in intensities can cause large changes in the electron density. This implies that it is very possible that the small field effects predicted can cause such an extreme flattening of these plasma balls. Additionally, we could investigate the effect of defect sites and how this would affect plasma formation.

Bibliography

[1] C L Arnold, A Heisterkamp, W Ertmer, and H Lubatschowski. Computational model for nonlinear plasma formation in high na micromachining of transparent materials and biological cells. *Optics Express*, 15(16), 2007.

[2] Paul R. Barnes and Frederick M. Tesche. On the direct calculation of a transient plane wave reflected from a finitely conducting half space. *IEEE Transactions on Electromagnetic Compatibility*, 33(2), 1991.

[3] V R Bhardwaj, P P Rajeev, P B Corkum, and D M Rayner. Strong field ionization inside transparent solids. *Journal of Physics B: Atomic, Molecular and Optical Physics*, 39, 2006.

[4] V R Bhardwaj, E Simova, P P Rajeev, C Hnatovsky, R S Taylor, D M Rayner, and P B Corkum. Optically produced arrays of planar nanostructures in fused silica. *Physical Review Letters*, 96, 2006.

[5] G T Boyd, T Rasing, J R R Leite, and Y R Shen. Local-field enhancement on rough surfaces of metals, semimetals and semiconductors with the use of optical second-harmonic generation. *Physical Review B*, 30(2):519–526, 1984.

[6] Robert W. Boyd. *Nonlinear Optics*. Academic Press, Oxford, 2003.

[7] Thomas Brabec. *Strong Field Laser Physics*. Springer, New York, 2008.

[8] E Bricchi, B G Klappauf, and P G Kazansky. Form birefringence and negative index change created by femtosecond direct writing in transparent materials. *Optics Letters*, 29(1), 2004.

[9] I M Burakov, N M Bulgakova, R Stoian, A Mermillod-Blondin, E Audouard, A Rosenfeld, A Husakou, and I V Hertel. Spatial distribution of refractive index variations induced in bulk fused silica by single ultrashort and short laser pulses. *Journal of Applied Physics*, 101, 2007.

[10] J. Burris and T. J. McIlrath. Theoretical study relating the two-photon absorption cross section to the susceptibility controlling four-wave mixing. *Journal of Optical Society of America B*, 2(8), 1985.

[11] J W Chan, T Huser, S Risbud, and D M Krol. Structural changes in fused silica after exposure to focused femtosecond laser pulses. *Optics Letters*, 26(21), 2001.

[12] Carl G Chen, Paul T Konkola, Juan Ferrera, Ralf K Heilmann, and Mark L Schattenburg. Analyses of vector gaussian beam propagation and the validity of paraxial and spherical approximations. *Journal of Optical Society of America A*, 19(2), 2002.

[13] David K. Cheng. *Field and Wave Electromagnetics*. Addison-Wesley Publishing Company, Reading, 1992.

[14] Paul Corkum. Private communication, 2008.

[15] Steven M. Cossmann, Edward J. Rothwell, and Leo C. Kempel. Transient reflection of te-polarized plane waves from a lorentz-medium half-space. *Journal of Optical Society of America A*, 23(9), 2006.

[16] Fumie Costen, Jean-Pierre Bergenger, and Anthony K. Brown. Comparison of fdtd hard source with fdtd soft source and accuracy assessment in debye media. *IEEE Transactions on Antennas and Propagation*, 57(7), 2009.

[17] K M Davis, K miura, N Sugimoto, and K Hirao. Writing waveguides in glass with a femtosecond laser. *Optics Letters*, 21(21), 1996.

[18] Q. Feng, J. V. Moloney, A. C. Newell, E. M. Wright, K. Cook, P. K. Kennedy, D. X. Hammer, B. A. Rockwell, and C. R. Thompson. Theory and simulation on the threshold of water breakdown induced by focused ultrashort laser pulses. *IEEE Journal of Quantum Electronics*, 33(2), 1997.

[19] L N Gaier, M Lein, M I Stockman, P L Knight, P B Corkum, M Yu Ivanov, and G L Yudin. Ultrafast multiphoton forest fires and fractals in clusters and dielectrics. *Journal of Physics B: Atomic, Molecular and Optical Physics*, 37, 2004.

[20] Rafael R Gattass and Eric Mazur. Femtosecond laser micromachining in transparent materials. *Nature*, 2, 2008.

[21] E N Glezer and E Mazur. Ultrafast-laser driven micro-explosions in transparent materials. *Applied Physics Letters*, 71(7), 1997.

[22] D Grojo, M Gertsvolf, H Jean-Ruel, S Lei, L Ramunno, D M Rayner, and P B Corkum. Self-controlled formation of microlenses by optical breakdown inside wide-band-gap materials. *Applied Physics Letters*, 93(243118), 2008.

[23] David Grojo. Private communication, 2008.

[24] D. Homoelle, S. Wielandy, Alexander L. Gaeta, N. F. Borrelli, and Charlene Smith. Infrared photosensitivity in silica glasses exposed to femtosecond laser pulses. *Optics Letters*, 24(18), 1999.

[25] T Q Jia, H X Chen, M Huang, and F L Zhao. Formation of nanogratings on the surface of a znse crystal irradiated by femtosecond laser pulses. *Physical Review B*, 72(125429), 2005.

[26] Rose M Joseph and Allen Taflove. Fdtd maxwell's equations models for nonlinear electrodynamics and optics. *Transactions on Antennas and Propagation*, 45(3), 1997.

[27] Saulius Juodkazis, Hiroaki Misawa, Egidijus Vanagas, and Mingwei Li. Simulation of light interaction with metallic nanoparticles. *Journal of Laser Micro/Nanoengineering*, 1(3), 2006.

[28] K G Kang, S H Lee, Y K Choi, and H-S Ryou. Fokker-planck approach to laser-induced damage in dielectrics with subpicosecond pulses. *Nanoscale and Microscale Thermophysical Engineering*, 10:217–232, 2006.

[29] Kwan Gu Kang, Seong Hyuk Lee, Young Ki Choi, Hong-Sun Ryou, Joon Sik Lee, and Seungho Park. Fokker-planck approach to laser-induced damage in dielectrics with subpicosecond pulses. *Nanoscale and Microscale Thermophysical Engineering*, 10:217–232, 2006.

[30] Peter G. Kazansky, Erica Bricchi, and Yasuhiko Shimotsuma an Kazuyuoki Hirao. Self-assembled nanostructures and two-plasmon decay in femtosecond processing of transparent materials. In *Proceedings of the 2007 Conference on Lasers and Electro-Optics/Quantum Electronics and Laser Science Conference*, Baltimore, Maryland, USA, April 2007.

[31] F Keilmann and Y H Bai. Periodic surface structures frozen into co_2 laser-melted quartz. *Applied Physics A*, 29:9–18, 1982.

[32] David F. Kelley and Raymond J. Luebbers. Piecewise linear recursive convolution for dispersive media using fdtd. *IEEE Transactions on Antennas and Propagation*, 44(6), 1996.

[33] Wolfgang Knoll. Interfaces and thin films as seen by bound electromagnetic waves. *Annual Review of Physics and Chemistry*, 49:569–638, 1998.

[34] E. Koushki, S. H. Mousavi, M. H. Majles Ara, and A. Koushki. Numerical simulation of a gaussian beam profile passing through a kerr medium. *Current Applied Physics*, 9:1347–1350, 2009.

[35] M Lezner, J Kruger, S Sartania, Z Cheng, Ch Spielmann, G Mourou, W Kautek, and F Krausz. Femtosecond optical breakdown in dielectrics. *Physical Review Letters*, 80(18), 1998.

[36] Raymond Luebbers, David Steich, and Karl Kunz. Fdtd calculation of scattering from frequency-dependent materials. *IEEE Transactions on Antennas and Propagation*, 41(9), 1993.

[37] Raymond J. Luebbers, Forrest Hunsberger, and Karl S. Kunz. A frequency-dependent finite-difference time-domain formulation for transient propagation in plasma. *IEEE Transactions on Antennas and Propagation*, 39(1), 1991.

[38] Raymond J. Luebbers, Forrest P. Hunsberger, Karl S. Kunz, Ronald B. Standler, and Michael Schneider. A frequency-dependent finite-difference time-domain formulation for dispersive materials. *IEEE Transactions on Electromagnetic Compatibility*, 32(3), 1990.

[39] Andrius Marcinkevicius, Saulius Juodkazis, Mitsuru Watanabe, Masafumi Miwa, Shigeki Matsuo, and Hiroaki Misawa. Femtosecond laser-assisted three-dimensional microfabrication in silica. *Optics Letters*, 26(5), 2001.

[40] Peter W. Milonni and Joseph H. Eberly. *Lasers*. John Wiley and Sons, New York, 1988.

[41] K miura, Jianrong Qiu, H Inouye, and T Mitsuyu. Photowritten optical waveguides in various glasses with ultrashort pulse laser. *Applied Physics Letters*, 71(23), 1997.

[42] Amit S. Nagra and Robert A. York. Fdtd analysis of wave propagation in nonlinear absorbing and gain media. *IEEE Transactions on Antennas and Propagation*, 46(3), 1998.

[43] Vaidya Nathan, A H Guenther, and S S Mitra. Review of multiphoton absorption in crystalline solids. *Journal of Optical Society of America B*, 2(2), 1985.

[44] Joachim Noack and Alfred Vogel. Laser-induced plasma formation in water at nanosecond to femtosecond time scales: calculation of thresholds, absorption coefficients, and energy density. *Journal of Quantum Electronics*, 35(8), 1999.

[45] Young Min Oh, Seong Hyuk Lee, S Park, and J S Lee. A numerical study on ultra-short pulse laser-induced damage on dielectrics using the fokker-planck equation. *International Journal of Heat and Mass Transfer*, 49:1493–1500, 2006.

[46] W. H. P. Pernice, F. P. Payne, and D. F. G. Gallagher. An fdtd method for the simulation of dispersive metallic structures. *Optical and Quantum Electronics*, 38:843–856, 2006.

[47] G M Petrov and J Davis. Interaction of intense ultra-short laser pulses with dielectrics. *Journal of Physics B: Atomic, Molecular and Optical Physics*, 41, 2008.

[48] P P Rajeev, M Gertsvolf, C Hnatovsky, E Simova, R S Taylor, P B Corkum, D M Rayner, and V R Bhardwaj. Transient nanoplasmonics inside dielectrics. *Journal of Physics B: Atomic, Molecular and Optical Physics*, 40, 2007.

[49] P P Rajeev, M Gertsvolf, E Simova, C Hnatovsky, R S Taylor, V R Bhardwaj, D M Rayner, and P B Corkum. Memory in nonlinear ionization of transparent solids. *Physical Review Letters*, 97(253001), 2006.

[50] D M Rayner, A Naumov, and P B Corkum. Ultrashort pulse non-linear optical absorption in transparent media. *Optics Express*, 13(9), 2005.

[51] B Rethfeld. Unified model for the free-electron avalanche in laser-irradiated dielectrics. *Physical Review Letters*, 92(18), 2004.

[52] B Rethfeld. Free-electron generation in laser-irradiated dielectrics. *Physical Review B*, 73, 2006.

[53] E A Romanova and A I Konyukhov. Study of irradiation conditions and thermodynamics of optical glass in the problem of modification of materials by femtosecond laser pulses. *Optics and Spectroscopy*, 104(5):784–790, 2008.

[54] J. E. Roy. A gaussian beam excitation for fdtd. *IEEE Antennas and Propagation Society International Symposium*, 3:118, 2002.

[55] Chris B Schaffer, Andre Brodeur, Jose F Gracia, and Eric Mazur. Micromachining bulk glass by use of femtosecond laser pulses with nanojoule energy. *Optics Letters*, 26(2), 2001.

[56] K. H. Schlereth and M. Tacke. The complex propagation constant of multilayer waveguides: an algorithm for a personal computer. *IEEE Journal of Quantum Electronics*, 26(4), 1990.

[57] Y. R. Shen. *The Principles of Nonlinear Optics*. John Wiley and Sons, Hoboken, 2003.

[58] Yasuhiko Shimotsuma, Peter G. Kazansky, Jiarong Qiu, and Kazuoki Hirao. Self-organized nanogratings in glass irradiated by ultrashort light pulses. *Physical Review Letters*, 91(24), 2003.

[59] Riaz Siushansian and Joe LoVetri. A comparison of numerical techniques for modeling electromagnetic dispersive media. *IEEE Microwave and Guided Wave Letters*, 5(12), 1995.

[60] S Skupin and L Berge. Self-guiding of femtosecond light pulses in condensed media: Plasma generation versus chromatic dispersion. *Physica D*, 220:14–30, 2006.

[61] R. E. Smith, S. N. houde Walter, and G. W. Forbes. Numerical determination of planar waveguide modes using the analyticity of the dispersion relation. *Optics Letters*, 16(17), 1991.

[62] Alexander M Streltsov and Nicholas F. Borrelli. Stude of femtosecond-laser-written waveguides in glasses. *Journal of Optical Society of America*, 19(10), 2002.

[63] B. C. Stuart, M. D. Feit, S. Herman, A. M. Rubenchik, B. W. Shore, and M. D. Perry. Nanosecond-to-femtosecond laser-induced breakdown in dielectrics. *Physical Review B*, 53(4), 1996.

[64] L. Sudrie, A. Couairon, M. Franco, B. Lamouroux, B. Prade adn S. Tzortzakis, and A. Mysyrowicz. Femtosecond laser-induced damage and filamentary propagation in fused silica. *Physical Review Letters*, 89(18), 2002.

[65] Dennis M. Sullivan. *Electromagnetic Simulation Using The FDTD Method*. Institute of Electrical and Electronics Engineers, Inc, New York, 2000.

[66] Nobuo Suzuki. Fdtd analysis of two-photon absorption and free-carrier absorption in si high-index-contrast waveguides. *Journal of Lightwave Technology*, 25(9), 2007.

[67] Allen Taflove and Susan C. Hagness. *Computational Electrodynamics: The Finite-Difference Time-Domain Method*. Artech House, Inc, Boston, 2005.

[68] R S Taylor, C hnatovsky, E Simova, D M Rayner, V R Bhardwaj, and P B Corkum. Femtosecond laser fabrication of nanostructures in silica glass. *Optics Letters*, 28(12), 2003.

[69] G Della Valle, R Osellame, and P Laporta. Micromachining of photonic devices by femtosecond laser pulses. *Journal of Optics A: Pure and Applied Optics*, 11, 2009.

[70] N. Yu. Vislobokov. Quasi-soliton and multifocal propagation in high-intensity laser pulses in silica glass. *Quantum Electronics*, 36(8):773–777, 2006.

[71] D. von der Linde and H. Schuler. Breakdown threshold and plasma formation in femtosecond laser-solid interaction. *Journal of Optical Society of America B*, 13(1), 1996.

[72] A Q Wu, I H Chowdhury, and X Xu. Femtosecond laser absorption in fused silica: Numerical and experimental investigation. *Physical Review B*, 72, 2005.

[73] Irina N. Zavestovskaya, Peter G. Eliseev, Oleg N. Krokhin, and Natalia A. Men'kova. Analysis of the nonlinear absorption mechanisms in ablation of transparent materials by high-intensity and ultrashort laser pulses. *Applied Physics A: Materials Science and Processing*, 92:903–906, 2008.

[74] Anatoly V. Zayats, Igor I. Smolyaninov, and Alexei A. Maradudin. Nano-optics of surface plasmon polaritons. *Physical Reports*, 408:131–314, 2005.